Electron irradiation effects on superconductivity in PdTe_2: an application of a generalized Anderson theorem

E. I. Timmons, S. Teknowijoyo, M. Kończykowski, O. Cavani, M. A. Tanatar, Sunil Ghimire, Kyuil Cho, Yongbin Lee, Liqin Ke, Na Hyun Jo, et al.

▶ **To cite this version:**

E. I. Timmons, S. Teknowijoyo, M. Kończykowski, O. Cavani, M. A. Tanatar, et al.. Electron irradiation effects on superconductivity in PdTe_2: an application of a generalized Anderson theorem. Physical Review Research, 2020, 2 (2), pp.023140. 10.1103/PhysRevResearch.2.023140 . hal-03800399

HAL Id: hal-03800399
https://hal.science/hal-03800399

Submitted on 6 Oct 2022

HAL is a multi-disciplinary open access archive for the deposit and dissemination of scientific research documents, whether they are published or not. The documents may come from teaching and research institutions in France or abroad, or from public or private research centers.

L'archive ouverte pluridisciplinaire **HAL**, est destinée au dépôt et à la diffusion de documents scientifiques de niveau recherche, publiés ou non, émanant des établissements d'enseignement et de recherche français ou étrangers, des laboratoires publics ou privés.

Distributed under a Creative Commons Attribution 4.0 International License

Electron irradiation effects on superconductivity in $PdTe_2$: An application of a generalized Anderson theorem

E. I. Timmons,[1,2] S. Teknowijoyo,[1,2] M. Kończykowski,[3] O. Cavani,[3] M. A. Tanatar,[1,2] Sunil Ghimire,[1,2] Kyuil Cho,[1] Yongbin Lee,[1] Liqin Ke,[1] Na Hyun Jo,[1,2] S. L. Bud'ko,[1,2] P. C. Canfield,[1,2] Peter P. Orth,[1,2] Mathias S. Scheurer,[4] and R. Prozorov[1,2,*]

[1]*Ames Laboratory, Ames, Iowa 50011, USA*

[2]*Department of Physics and Astronomy, Iowa State University, Ames, Iowa 50011, USA*

[3]*Laboratoire des Solides Irradiés, CEA/DRF/IRAMIS, Ecole Polytechnique, CNRS, Institut Polytechnique de Paris, F-91128 Palaiseau, France*

[4]*Department of Physics, Harvard University, Cambridge, Massachusetts 02138, USA*

(Received 29 January 2020; revised manuscript received 16 March 2020; accepted 17 March 2020; published 8 May 2020)

Low-temperature (∼20 K) electron irradiation with 2.5 MeV relativistic electrons was used to study the effect of controlled nonmagnetic disorder on the normal and superconducting properties of the type-II Dirac semimetal $PdTe_2$. We report measurements of longitudinal and Hall resistivity, thermal conductivity and London penetration depth using the tunnel-diode resonator technique for various irradiation doses. The normal-state electrical resistivity follows the Matthiessen rule with an increase of the residual resistivity at a rate of $\sim 0.77\ \mu\Omega\,\mathrm{cm}/(\mathrm{C}/\mathrm{cm}^2)$. London penetration depth and thermal conductivity results show that the superconducting state remains fully gapped. The superconducting transition temperature is suppressed at a nonzero rate that is about 16 times slower than described by the Abrikosov-Gor'kov dependence, applicable to magnetic impurity scattering in isotropic, single-band *s*-wave superconductors. To gain information about the gap structure and symmetry of the pairing state, we perform a detailed analysis of these experimental results based on insight from a generalized Anderson theorem for multiband superconductors. This imposes quantitative constraints on the gap anisotropies for each of the possible pairing candidate states. We conclude that the most likely pairing candidate is an unconventional A_{1g}^{+-} state. While we cannot exclude the conventional A_{1g}^{++} and the triplet A_{1u}, we demonstrate that these candidates require additional assumptions about the orbital structure of the disorder potential to be consistent with our experimental results, e.g., a ratio of inter- to intraband scattering for the singlet state significantly larger than 1. Due to the generality of our theoretical framework, we believe that it will also be useful for irradiation studies in other spin-orbit-coupled multiorbital systems.

DOI: 10.1103/PhysRevResearch.2.023140

I. INTRODUCTION

The layered transition-metal dichalcogenide (TMD) superconductor $PdTe_2$ [1,2] has received renewed interest recently after the discovery of type-II Dirac points in its bulk band structure [3]. As shown by angle-resolved photoemission (ARPES) and density functional theory (DFT) calculations [4,5], the nodal points, which are protected by threefold rotation symmetry, lie about 0.6 eV below the Fermi energy E_F and occur along the Γ-A line in the Brillouin zone. The Fermi surface consists of several electron pockets around the K and K' points and two hole pockets around Γ, whose energy bands eventually cross at the Dirac point. A proposed mechanism that can explain the occurrence of this crossing [6] invokes a band inversion of chalcogenide p states in this strongly spin-orbit-coupled material, and it was shown to be relevant for a number of other TMDs as well.

$PdTe_2$ becomes superconducting below a transition temperature of $T_c = 1.7$ K [1,2]. The superconducting state was consistently found to be fully gapped in a number of experiments performing thermodynamic [7], penetration depth [8], scanning tunnel microscopy (STM) [9], and heat capacity [10] measurements. Superconductivity was reported to be of type-I based on magnetization [7] and muon spin rotation [11] studies. This is consistent with an experimentally observed Ginzburg ratio of $\kappa = \xi/\lambda \simeq 0.52 < 1/\sqrt{2}$, when ξ and λ are directly extracted from critical field $H_c(0)$ [7] and penetration depth [8] measurements, respectively.

The presence of strong spin-orbit coupling and band inversions provides a natural motivation for a detailed investigation of the symmetry of the superconducting pairing state in this multiband system. In a previous work, Teknowijoyo *et al.* [8] performed a systematic classification of all possible translationally invariant superconducting pairing states in $PdTe_2$ based on its point group D_{3d}. Using the condition of a full gap

*Author to whom all correspondence should be addressed: prozorov@ameslab.gov

Published by the American Physical Society under the terms of the Creative Commons Attribution 4.0 International license. Further distribution of this work must maintain attribution to the author(s) and the published article's title, journal citation, and DOI.

left only three candidates remaining: an *s*-wave superconductor that transforms trivially under all lattice symmetries (A_{1g}), an odd-parity *p*-wave triplet state (A_{1u}), and a generically anisotropic triplet state $e_{u(1,0)}$. While the *s*-wave state is topologically trivial, the two odd-parity superconducting phases can exhibit nontrivial topology depending on the relative sign of the gap on the different Fermi pockets.

One well-known approach to obtain further insight into the pairing symmetry is to investigate the behavior of the superconducting phase under tuning the amount of disorder in the system. In particular, the rate at which the transition temperature T_c changes with the disorder level can provide information about the pairing state. This technique was successfully applied to various superconducting materials, for example to the cuprates, ruthenates, and the iron-based superconductors [12–18]. Here, we use electron irradiation to study the impact of nonmagnetic disorder on the superconducting and the normal state in single crystals of $PdTe_2$. Irradiation with relativistic electrons in the MeV energy range at low temperatures (at about 20 K) is known as the cleanest and most controllable way to create point defects, predominantly in the form of vacancies and interstitials [19]. Employing a combination of transport and London penetration depth measurements using a tunnel diode resonator (TDR) technique [20,21], we find that the superconducting state remains fully gapped after irradiation. We observe that the transition temperature T_c is suppressed with increasing levels of disorder, yet the rate of suppression is found to be notably lower than predictions of the Abrikosov-Gor'kov (AG) theory for magnetic impurity scattering in *s*-wave superconductors [22].

To interpret these experimental observations, one notes that, since the early work of Anderson [23], and Abrikosov and Gor'kov [24,25], it is known that the superconducting state can enjoy protection against certain forms of disorder that obey appropriate symmetries: the transition temperature T_c of a single-band *s*-wave superconductor with an isotropic gap is independent of the amount of nonmagnetic, i.e., time-reversal symmetric (TRS), disorder. This phenomenon is commonly referred to as the "Anderson theorem." In contrast, T_c is reduced by the presence of magnetic impurities, i.e., time-reversal antisymmetric (TRA) disorder. For a single-band, isotropic *s*-wave superconductor, T_c then follows the well-known AG law [22]. This is different for anisotropic gap functions, e.g., with (anisotropic) *s*-, *p*-, or *d*-wave symmetry, for which T_c is sensitive to TRS disorder already [26–34]. The decrease of T_c as a function of an increasing scattering rate off nonmagnetic impurities is therefore often (yet sometimes wrongly) regarded as a signature of unconventional superconductivity.

The situation in multiorbital and multiband unconventional superconductors is significantly more rich [32]. For example, the gap function can take different values [35] or even different signs [36,37], on different Fermi pockets, leading to a different sensitivity with respect to inter- and intraband scattering processes [38–40]. Furthermore, spin-orbit coupling has been demonstrated to be able to enhance the stability of the superconducting state against disorder in both centrosymmetric [41,42] and noncentrosymmetric [43] multiorbital systems. Interestingly, a generalization of the Anderson theorem for the multiorbital and multiband case has recently been derived [44,45], which shows that unconventional pairing states can also enjoy protection against certain forms of disorder. For instance, a two-band superconductor with a sign-changing s^{+-} gap function is protected against TRA interband scattering as long as the size of the gap is equal on both Fermi surfaces [44].

In Ref. [45], the general form of this Anderson theorem was derived and expressed in terms of (anti)commutators of the superconducting order parameter, the disorder potential, and the normal-state Hamiltonian, thus assuming a purely algebraic form that can be readily applied in any basis. We will review this form of the generalized Anderson theorem; we show that the rate at which T_c decreases with increasing scattering strength is determined by a Fermi-surface average of precisely the same (anti)commutator that also enters the generalized Anderson theorem. As a result, if the (anti)commutator relations are only weakly violated, T_c decreases slowly and superconductivity is significantly more protected than described by the AG law. We will see how special cases of the expression for the reduction of T_c reproduce well-known results of the literature.

The presence of strong spin-orbit coupling can largely suppress the rate at which T_c decreases with disorder [41–43,45]. This results from a mixing of spin and orbital degrees of freedom that can potentially lead to a reduced overlap of the wave functions of scattering partners under the natural assumption that impurity scattering acts trivially in orbital space. Michaeli and Fu have shown in a $\boldsymbol{k}\cdot\boldsymbol{p}$ model relevant to doped Bi_2Se_3 that if the normal-state Hamiltonian obeys an additional symmetry, such "spin-orbit locking" can even lead to a complete protection against disorder for fully gapped odd-parity superconductors [41]. We will see below that this result readily follows from the generalized Anderson theorem of Ref. [45], revealing the general conditions for symmetry-enhanced protection of superconductivity against disorder.

Based on these insights, and since the Fermi surface in $PdTe_2$ consists of several electron and two hole pockets, we analyze our experimental result of weak T_c suppression under irradiation within the framework of this generalized Anderson theorem. This allows us to describe the different pairing scenarios within one framework. We employ the experimentally measured slope of the T_c suppression with increasing scattering to make quantitative predictions on the properties of the different pairing state candidates. For instance, an *s*-wave pairing state that has the same sign on all Fermi surfaces, denoted by A_{1g}^{++} below, must exhibit a rather substantial degree of momentum dependence of the superconducting gap to be consistent with the data. More precisely, the ratio of gaps on different Fermi sheets must be at least 2. Finally, the odd-parity A_{1u} pairing is only consistent with the data if the bands that make up the Fermi surface exhibit a substantial mixing of even- and odd-parity wave functions. This work exemplifies the predictive power of this combined experimental-theoretical approach to constrain the microscopic superconducting order parameter by controllably tuning the amount of nonmagnetic disorder. At the same time, it also highlights important caveats in the interpretation of disorder-induced suppression of T_c in multiorbital systems with strong spin-orbit coupling.

The remainder of this paper is organized as follows. In Sec. II, we describe the experimental details of our measurements. Our experimental results of resistivity, Hall effect measurements, thermal transport, and London penetration depth before and after electron irradiation are presented in Sec. III. We discuss and interpret these results in Sec. IV within the various possible superconducting pairing symmetries of the system. This allows us to draw quantitative conclusions, e.g., on the required degree of the superconducting gap anisotropy, and we impose quantitative restrictions on the properties of the different pairing states based on our experimental results. We conclude in Sec. V and present details of the theoretical derivations and first-principles density functional theory (DFT) calculations in the Appendixes.

II. EXPERIMENTAL DETAILS

Single crystals of $PdTe_2$ were grown using a procedure described in our earlier work [8]. Samples used for four-probe in-plane electrical resistivity, ρ, and thermal conductivity, κ, measurements and for five-probe Hall effect measurements were cleaved from the inner parts of large single crystals with typical dimensions of (2–3) × 0.5 × 0.05 mm^3. The longer side of the sample was along an arbitrary direction in the hexagonal crystal plane. Contacts to the fresh cleaved surface of the samples were made by attaching 50 μm silver wires with In solder [46]. The same samples were used before and after irradiation thus essentially eliminating the relatively large uncertainty associated with determining the geometric factor. The resistivity of the pristine samples at room temperature was set at 24 $\mu\Omega$ cm as determined by a statistically significant average on a large array of crystals in our previous study [8]. Temperature-dependent electrical resistivity and thermal conductivity measurements were made in two setups, PPMS (1.8–300 K) and a cryogen-free Janis ^{3}He system (0.5–3 K). A modular thermal conductivity device was used [47], enabling measurements in both systems without dismounting the sample. For the Hall effect measurements, the sample contacts were soldered to the side surfaces of a 67-μm-thick sample. Measurements were performed in a PPMS device using magnetic field sweeps in the range −9 to 9 T at selected constant temperatures. The Hall resistance was determined as the difference between measurements in inverted magnetic fields.

We performed precision measurements of the in-plane London penetration depth $\Delta\lambda(T)$ using the tunnel-diode resonator (TDR) technique [20]. Measurements were conducted in a high-stability ^{3}He cryostat with a base temperature of ∼0.4 K. One sample was measured multiple times before and after electron irradiation. The sample was placed with its c-axis parallel to an excitation field, $H_{ac} \sim 20$ mOe, which is much smaller than H_{c1} [7]. The shift of the resonance frequency, $\Delta f(T) = -G4\pi\chi(T)$, is proportional to the differential magnetic susceptibility $\chi(T)$. The constant $G = f_0V_s/2V_c(1-N)$ depends on the demagnetization factor N, sample volume V_s, and coil volume V_c. The constant G was determined experimentally from the full frequency change that occurs when the sample is physically pulled out of the coil. To obtain the (change of the) London penetration depth $\Delta\lambda(T)$ as a function of temperature, we use the expression $4\pi\chi = (\lambda/R)\tanh(R/\lambda) - 1$ [21,48]. Here, R is an effective sample size that can be calculated and depends on the sample geometry, and $\chi(T)$ is the experimentally measured magnetic susceptibility.

Electron irradiation was performed at the SIRIUS Pelletron linear accelerator in Laboratoire des Solides Irradiés at École Polytechnique in Palaiseau, France. Relativistic electrons with an energy of 2.5 MeV were used to create pointlike defects (Frenkel pairs) by knocking the ions away from the regular position in the lattice [49,50]. Details regarding electron irradiation and its influence on Fe-based superconductors can be found elsewhere [50]. The defect concentration produced by irradiation with electrons with energies in the MeV range is homogeneous throughout the sample thickness as long as it is smaller than the large electron penetration depth (2.3 mm for 2.5 MeV electron energy) [51]. The homogeneous damage of our samples can be seen directly from the fact that the superconducting transitions remain sharp after irradiation. The acquired irradiation dose presented in this paper is in units of Coulomb per square centimeter, where 1 C/cm^2 = 6.24 × 10^{18} electrons/cm^2. The total charge of electrons penetrated through the sample was measured by a Faraday cage placed behind the sample stage.

Contacts to the samples for transport measurements deteriorate after irradiation, resulting in a higher noise level. For this reason, all transport measurements with different irradiation doses (0.91, 1.75, and 2.41 C/cm^2 for resistivity, 0.91 C/cm^2 for thermal conductivity, and 1.33 C/cm^2 for Hall effect) were made on individual samples, comparing pristine (before irradiation) and irradiated states. The T_c for the sample with an irradiation dose of 1.75 C/cm^2 was not determined. Multiple irradiation cycles allowing for accumulation of notably higher doses were used for samples used in penetration depth measurements, invoking no contact making.

III. EXPERIMENTAL RESULTS

A. Electrical resistivity

We have measured longitudinal and Hall resistivity as a function of temperature and magnetic field, both before and after irradiation. The main panel of Fig. 1 shows the temperature-dependent in-plane resistivity ρ of $PdTe_2$ before (black and gray) irradiation and after irradiations with the doses of 0.91 C/cm^2 (red curve) and 2.41 C/cm^2 (magenta curves). The observed temperature dependence is typical of a good metal with a range of nearly temperature-independent resistivity below 10 K and a linear increase of ρ with T above 40 K. The response of the sample resistivity to disorder introduced by electron irradiation is also typical of a simple metal. As expected from the Matthiessen rule, the curves for 0.91 C/cm^2 irradiation shift up parallel to themselves due to an increase of residual resistivity from $\rho^{(\text{pristine})}(0) = 0.6\ \mu\Omega$ cm to $\rho^{(2.41\ \text{C/cm}^2)}(0) = 2.3\ \mu\Omega$ cm; see panel (b). The resistivity difference of the irradiated and pristine samples, $\rho(0.91\ \text{C/cm}^2) - \rho(0\ \text{C/cm}^2)$, as shown with a blue line in the main panel (a) of Fig. 1 magnified by a factor of 10, is almost temperature-independent. For the sample with 2.41 C/cm^2 irradiation (dark magenta line) the shift is not parallel, and the slope of the line above 40 K increases. This observation suggests that the geometric factor of the sample

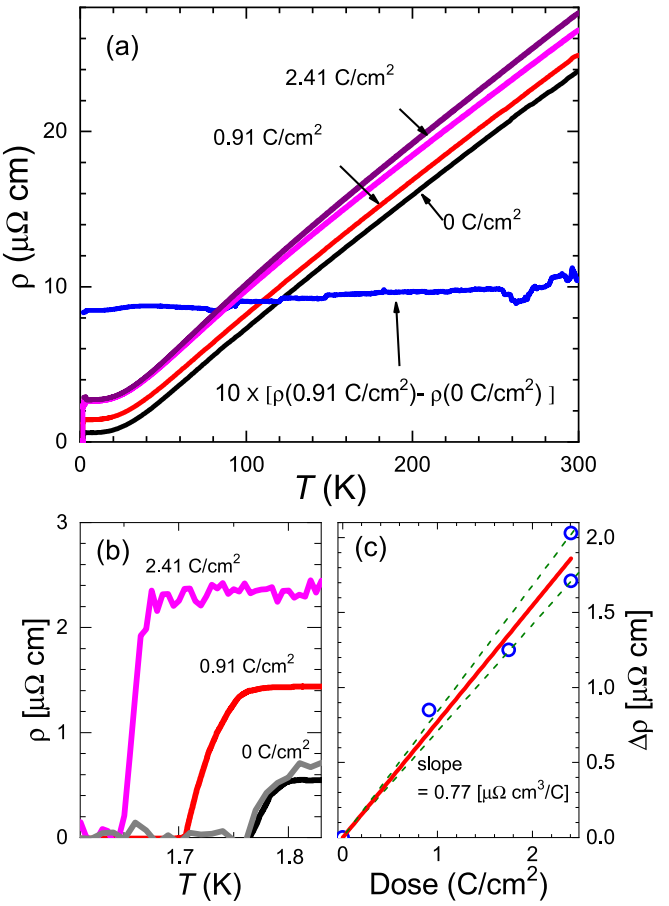

FIG. 1. (a) Temperature-dependent in-plane electrical resistivity of $PdTe_2$ before (black and gray curves) and after low-temperature electron irradiations of 0.91 (red) and 2.41 C/cm^2 (magenta), together with the difference between resistivities of the pristine and 0.91 C/cm^2 irradiated samples (multiplied by a factor of 10, blue curve). The data for the 2.41 C/cm^2 sample after irradiation do not show a parallel $\rho(T)$ curve shift, indicating a change of the geometric factor. Correction using a normalized $\rho(T)$ curve slope near room temperature makes the 2.41 C/cm^2 sample look like a smooth parallel upshift of 0.91 C/cm^2 (light magenta curve). (b) The zoom of the superconducting transition range with T_c suppression by 0.06 K and ~0.11 K using a resistivity offset criterion and a residual resistivity increase from 0.6 to 2.3 $\mu\Omega$ cm, from pristine to 2.41 C/cm^2. (c) The resistivity increase as a function of irradiation dosage. For the sample with 2.41 C/cm^2 dose we use resistivity above T_c without (top point) and with (bottom point) geometrical factor correction. The straight red line shows a linear fit through all data points with a slope of 0.77 ± 0.07 $\mu\Omega$ per C/cm^2, while the green dashed lines show the slopes for the error bar ranges.

changed during irradiation due to crack formation [50]. Partially this effect can be removed by normalizing the slope of the curve at high temperature to that before irradiation (light magenta curve). This brings approximately 10% uncertainty to the residual resistivity of the 2.41 C/cm^2 irradiated sample. In panel (c) we show an increase of residual resistivity with irradiation dose. For the 2.41 C/cm^2 sample we show two values as determined from direct measurements (top point) and from the slope-normalized curve (bottom point). The dependence of $\rho(0)$ on dose is close to linear, as expected

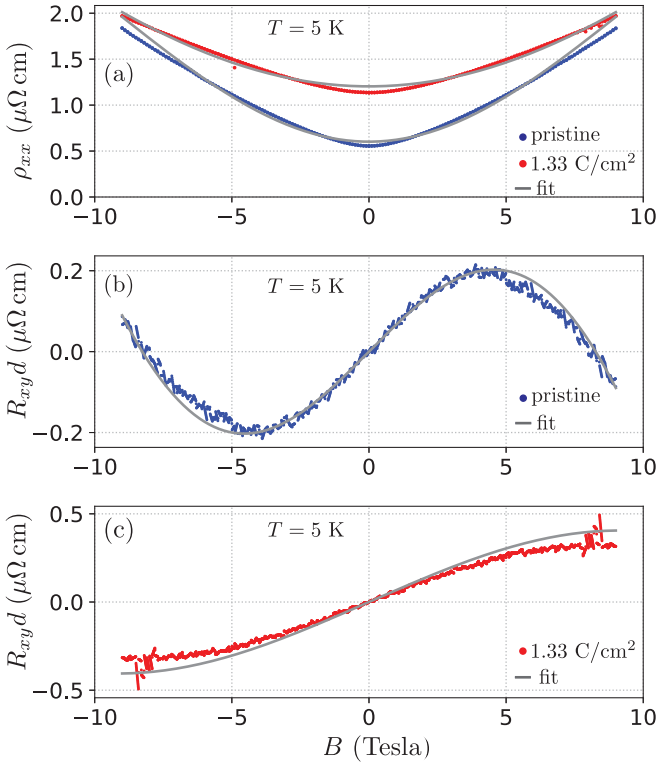

FIG. 2. (a) Low-temperature longitudinal resistivity ρ_{xx} as a function of magnetic field $B = \mu_0 H$ at $T = 5$ K. The blue (red) line shows the result for the pristine sample (irradiated with a dose 1.33 C/cm^2) and the gray line is the two-band model fit. (b), (c) Low-temperature Hall resistance R_{xy} multiplied by sample thickness $d = 67$ μm as a function of magnetic field B of the pristine sample (blue, panel b), the irradiated sample (red, panel c), together with the two-band model fit (gray).

and observed in samples continuously measured *in situ* at low temperatures [64]. Due to variation of the geometric factor, the slope of the curve is determined by a linear fit through data points with onset fixed at (0,0) (red curve) as 0.77 $\mu\Omega$ cm per C/cm^2. Green dashes show error bars of slope determination. We use the linear dependence of residual resistivity on dose with the slope of 0.77 $\mu\Omega$ cm/(C/cm^2) for determination of resistivity in samples used in penetration depth studies; see Fig. 1(c). Importantly, the superconducting transition is equally sharp before and after irradiation treatments, with a full width of just 0.05 K from the onset to zero resistivity. The transition temperature T_c is suppressed by 0.06 K as a result of irradiation with a dose of 0.91 C/cm^2 and by 0.11 K for a dose of 2.41 C/cm^2.

In Fig. 2, we show the longitudinal resistivity ρ_{xx} and transverse Hall resistance multiplied by the sample thickness d, $R_{xy}d$, as a function of magnetic field at low temperatures $T = 5$ K, both before and after electron irradiation with a dose of 1.33 C/cm^2. To extract the carrier densities and mobilities, we perform a fit to standard expressions of ρ_{xx} and ρ_{xy} for a two-band model of electron and hole charge carriers (for details, see Appendix C) [52]. For the pristine sample, the optimal fit parameters are $n_e^{(\text{pristine})} = 4.2(1) \times 10^{27}$ m^{-3} and $n_h^{(\text{pristine})} = 2.2(1) \times 10^{27}$ m^{-3} for the electron and hole densities, and $\mu_e^{(\text{pristine})} = 0.10(1)$ m^2/V s and

$\mu_h^{(\text{pristine})} = 0.28(1)$ m^2/V s for the electron and hole mobilities. After irradiation with a dose of 1.33 C/cm^2, the densities n_e and n_h are unchanged, and the mobilities are reduced by approximately a factor of 2: $\mu_e^{(1.33\ \text{C/cm}^2)} = 0.05(1)$ m^2/V s and $\mu_h^{(1.33\ \text{C/cm}^2)} = 0.14(1)$ m^2/V s. Note that we have used units of m^2/Vs for mobilities here. This is consistent with our observation that the Hall constant $R_H = d\frac{\partial R_{xy}}{\partial B}(B = 0)$ at low temperatures is unchanged during irradiation with this dose. We note that $R_H = 0.60(5)$ mm^3/C is approximately independent of temperature in the pristine sample.

Using the bare electron mass, we can extract a rough estimate of the scattering rates $h/\tau_e = he_0/(m_e\mu_e) = 70(2)$ meV and $h/\tau_h = 26(2)$ meV of the pristine sample. The rates are a factor of 2 larger after irradiation. Using the approximation of a three-dimensional quadratic dispersion, we find mean free paths of $\ell_e = 172(5)$ nm and $\ell_h = 363(5)$ nm for electron and hole charge carriers after irradiation (with dose 1.33 C/cm^2). Note that this is of the same order as the superconducting coherence length $\xi = 439$ nm, reported in the material [7,8]. Importantly, this corresponds to a small disorder parameter $k_F\ell_e = 860(5)$ and $k_F\ell_h = 145(5)$ for electrons and holes, respectively, justifying the perturbative treatment of disorder we use below.

B. Thermal transport

We have measured the thermal conductivity κ in $PdTe_2$ before and after irradiation with a dose of 0.91 C/cm^2. Measurements of κ were made in a temperature range from $T = 0.5$ to 3 K using MTC units in a cryogen-free He3 setup (see Sec. II). In the normal state, above T_c, we observe that κ is related to the electrical conductivity $\sigma = 1/\rho$ via the Wiedemann-Franz (WF) law $\kappa/\sigma = L_0T$ within experimental scatter of the data to an accuracy of better than 10%; see the inset in Fig. 3. Here, $L_0 = \frac{\pi^2}{3}(\frac{k_B}{e})^2 = 2.45 \times 10^{-8}$ W Ω K^{-2} is the Sommerfeld value of the Lorenz number [53–55]. This shows that the phonon contribution to the thermal conductivity is negligible in the normal state. The WF law is obeyed in both the pristine and the irradiated sample.

In the superconducting state, the WF law is grossly violated because the superfluid part of the conduction electron density does not contribute to thermal conductivity. The electronic part of thermal conductivity is determined by the residual electronic excitations, which in the case of a fully gapped superconductor are exponentially suppressed as $T \to 0$ [54]. Therefore, a straightforward way to distinguish between nodal and full-gap superconductors is to extrapolate $\kappa(T)$ to its value as $T \to 0$. For a nodal superconductor, this extrapolation yields a finite positive value [56], while κ/κ_N extrapolates to a (physically meaningless) negative value in the full-gap case. The contribution of phonons in more disordered samples is more significant, which makes this extrapolation to negative value less convincing in the sample subjected to 0.91 C/cm^2 electron irradiation.

In Fig. 3, we plot the thermal conductivity normalized by its value at T_c, $\kappa_S(T)/\kappa_N(T_c)$, which shows that κ extrapolates to a negative value, corresponding to a full gap, for both pristine and irradiated samples of $PdTe_2$. For comparison, we plot the thermal conductivities of Al [57], a clean fully gapped superconductor, which shows negative $\kappa_S(T)/\kappa_N(T_c)$ extrapolation $T \to 0$, and the nodal superconductor $CeIrIn_5$ [58,59] for samples of different disorder level. In the nodal case, the curve extrapolates to a finite positive value [59–61] rapidly increasing for samples with large residual resistivity [59,61]; compare the curves for samples with $\rho(0) \sim 0.2$ and 0.5 μΩ cm.

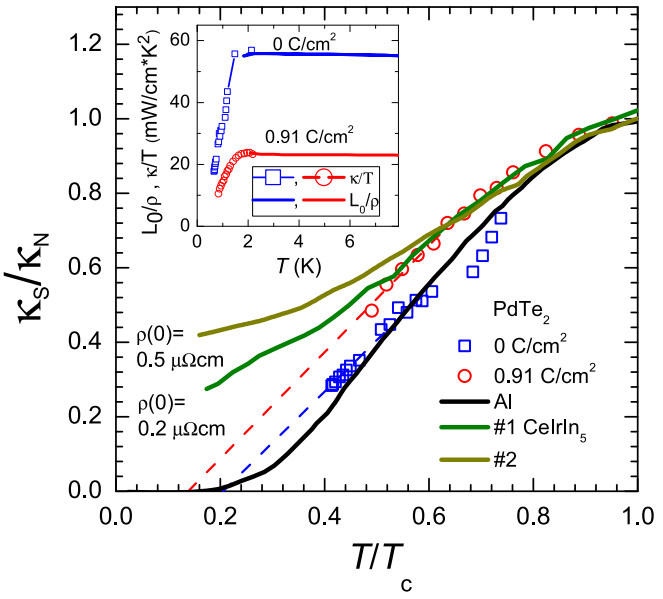

FIG. 3. Inset: comparison of thermal conductivity, κ/T (symbols), and electrical resistivity data converted to equivalent thermal conductivity by using the WF law, L_0/ρ (lines). The two data sets coincide within the accuracy of our measurements above T_c in both pristine (blue) and irradiated (red) samples. Main panel: ratio of thermal conductivity in the superconducting and normal states, $\kappa_S(T)/\kappa_N(T_c)$, plotted vs reduced temperature T/T_c. Open blue squares and red circles are the data for pristine and electron-irradiated $PdTe_2$ with a dose 0.91 C/cm^2. The blue and red dashed lines are linear fits to the low-temperature part of the data, showing extrapolation toward a negative value, suggesting a fully gapped superconducting state. For comparison, we show data for the conventional full-gap superconductor Al [57] extrapolating to a negative value, and the nodal superconductor $CeIrIn_5$ [58] for samples with different quality as characterized by the residual normal-state resistivity of ∼0.2 μΩ cm (green line) and ∼0.5 μΩ cm (dark yellow line), with linear extrapolation to a finite ratio as $T \to 0$.

C. London penetration depth

In the main panel of Fig. 4, we present the temperature-dependent London penetration depth $\Delta\lambda$, measured over the whole range of superconductivity. In the pristine sample, the superconducting transition occurs at temperature T_c(onset)1.76 K. Note that the onset T_c in penetration depth is consistent with the offset T_c in resistivity. The transition is sharp and highly reproducible, as expected in stoichiometric materials. Upon a series of electron irradiations with doses of 0.91 C/cm^2 (2.5 MeV), plus 2.07 C/cm^2 (2.2 MeV), and plus 4.25 C/cm^2 (2.5 MeV), the transition temperature continuously decreases from 1.76 to 1.70 K (for a dose of 0.91 C/cm^2) to 1.66 K (for an additional dose of 2.07 C/cm^2) to 1.59 K (for an additional dose of 4.25 C/cm^2). This

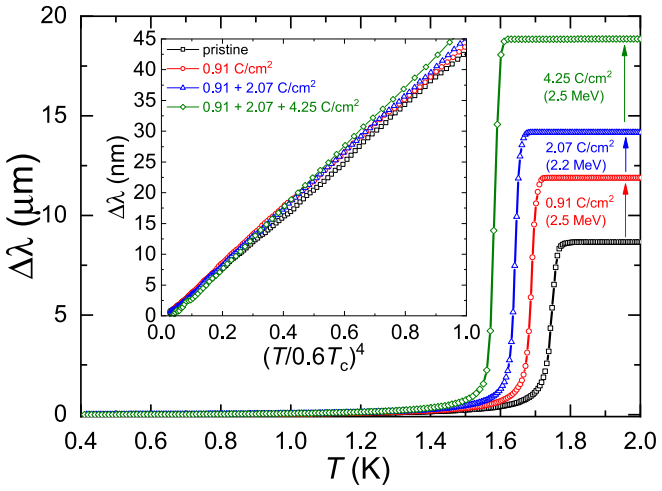

FIG. 4. Temperature variation of London penetration depth $\Delta\lambda(T)$ measured in a ^{3}He TDR setup before and after irradiations. The main panel displays data over the whole temperature range that clearly shows the suppression of T_c and an increase of normal-state skin depth ($T > T_c$). The inset shows the low-temperature penetration depth below $0.6T_c$ plotted as a function of T^4, which reveals the exponential behavior of BCS-type full gap structure even after three irradiations.

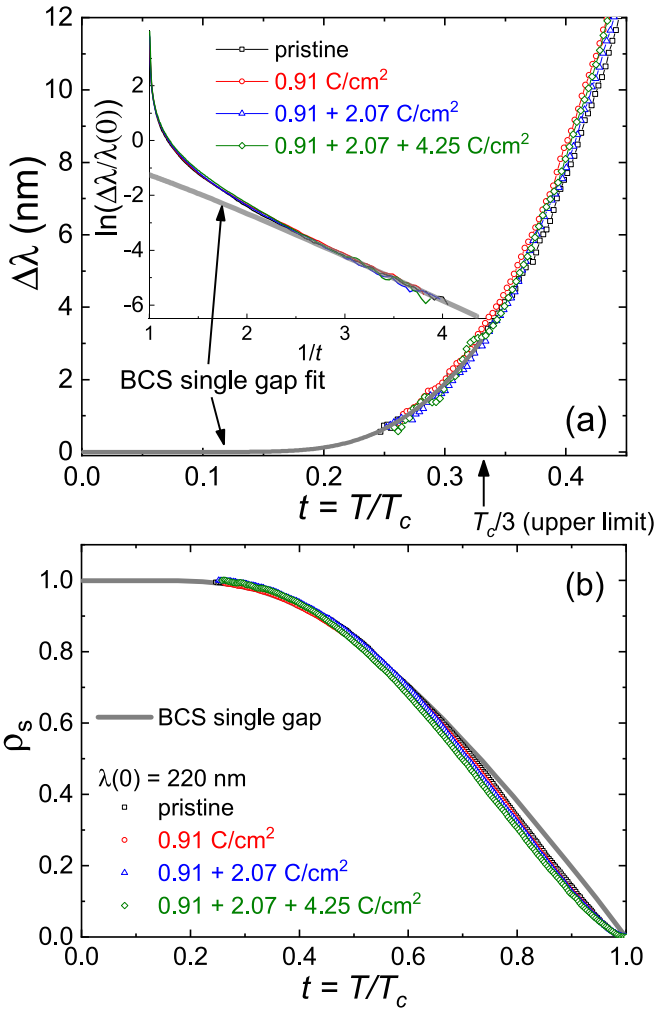

FIG. 5. (a) The low-temperature region of London penetration depth before and after irradiations (identical sample in Fig. 4). All data are well-fitted with a BCS single gap function. (b) Superfluid density calculated from $\Delta\lambda$ in panel (a), $\rho_s(T) \equiv [\lambda(0)/\lambda(T)]^2$, which is found to be only very weakly affected by irradiation.

corresponds to a decrease by about 9.6% in total. The increase of the penetration height above $T > T_c$ upon irradiation is caused by an increase of the normal state skin depth and is consistent with the observed increase of residual resistivity $\rho(0)$ from a direct measurement in Fig. 1.

The inset of Fig. 4 shows $\Delta\lambda(T)$ at low temperatures before and after irradiation. We see that $\Delta\lambda \propto (T/T_c)^4$ over the range up to $0.6T_c$ in both the pristine state and after two irradiations. It is quite remarkable that despite the notable T_c suppression, the functional dependence of $\Delta\lambda$ on the temperature is almost unchanged at low temperatures and remains $\propto T^4$. In the temperature range that we consider, a power-law function with exponent $n \simeq 4$ cannot be distinguished from an exponential function. An exponential decrease of $\Delta\lambda(T)$ is expected in a clean and fully gapped BCS superconductor [62]. In contrast, in the presence of line nodes in the gap, one rather expects a close to T-linear decay of $\Delta\lambda$. In both cases, the behavior changes to T^2 under the addition of sufficiently strong disorder [17]. Note that our study is not performed within this strong disorder regime, and $\Delta\lambda$ remains $\propto T^4$ for all irradiation doses.

It is important to restrict the fit of $\Delta\lambda$ to a low-temperature region below $0.33T_c$, where the temperature dependence of the superconducting gap magnitude is negligible (in single-gap superconductors) and the T-dependence is determined by thermal excitation of quasiparticles across the superconducting gap. In the top panel of Fig. 5, we show a fit of the penetration depth $\Delta\lambda$ using an exponential temperature dependence, which is expected from Bardeen-Cooper-Schrieffer (BCS) theory. We obtain an excellent fit using the single-gap isotropic BCS expression

$$\Delta\lambda(T) = \lambda(0)\sqrt{\frac{\pi\delta}{2t}}\exp(-\delta/t) \qquad (1)$$

with $\delta = \Delta/T_c = 1.76$ and $t = T/T_c$. The fit yields a zero-temperature value of $\lambda(0) = 220 \pm 15$ nm (pristine), 235 ± 15 nm (0.91 C/cm^2), and 214 ± 15 nm (0.91 + 2.07 C/cm^2). The data after 0.91 + 2.07 + 4.25 C/cm^2 show a higher noise level preventing us from a good fitting to get $\lambda(0)$. In the inset of Fig. 5(a), we also plot $\ln(\Delta\lambda/\lambda(0))$ versus $1/t$, clearly showing that all data are consistent with a BCS single-gap fit. We conclude that the zero-temperature penetration depth $\lambda(0)$ is approximately constant within error bars. This is in reasonable agreement with expectations based on $\lambda_{\rm eff}(\ell) = \lambda(0)(1 + \xi/\ell)^{1/2}$ [63], and using that the carrier densities are unchanged by irradiation [and $\lambda(0)$ thus remains unchanged] and $\ell_e, \ell_h \simeq \xi$. Our estimated mean free path $\bar{\ell}^{(\rm pristine)} \simeq 530$ nm (average of ℓ_e and ℓ_h) is of the same order as the superconducting coherence length $\xi = 439$ nm [7,8]. We thus expect that $\lambda(0)^{(\rm pristine)}/\lambda(0)^{(0.91\,{\rm C/cm^2})} \simeq 0.85$, while we find approximately $220/235 \simeq 0.94$. In the following, we work with an average value of $\lambda(0) = 220$ nm.

Having experimentally determined $\lambda(0)$ using the BCS fit, we can construct the temperature-dependent normalized superfluid density as $\rho_s(T) = [\lambda(0)/\lambda(T)]^2$, with $\lambda(T) = \lambda(0) + \Delta\lambda(T)$. In Fig. 5(b) we show the resulting superfluid density $\rho_s(T)$ before and after irradiation, which is calculated from our experimental data and using an average value of $\lambda(0) = 220$ nm. The data are plotted versus reduced temperature T/T_c and compared with BCS expectations for a single fully gapped superconductor (thick gray curve). The excellent agreement clearly shows that superconductivity in $PdTe_2$ can be well characterized by a *single* and full superconducting gap energy scale. Importantly, this observation sets rather stringent conditions on the amount of anisotropy of the gap magnitudes $|\Delta_\alpha|/|\Delta_\beta|$ that are consistent with this behavior, despite the rather substantial T_c suppression upon increasing disorder.

IV. DISCUSSION

In this section, we analyze our experimental results with the goal of determining the properties of the superconducting pairing state, for example its pairing symmetry and gap anisotropies. Our comprehensive analysis puts important quantitative constraints on the superconducting state in each of the possible full-gap pairing scenarios [8]. While we cannot definitely rule out any of the candidate states, our analysis points toward an unconventional spin-singlet A_{1g}^{+-} pairing state as the most likely candidate. Further work addressing microscopic details of disorder scattering caused by electron irradiation is suggested.

Let us briefly summarize the main experimental results presented in Sec. III. We have found that electron irradiation of $PdTe_2$ single crystals leads to a temperature-independent upward shift of the resistivity ρ that is caused by an increase in the residual resistivity $\Delta\rho_0$, which is proportional to the irradiation dose. Analyzing Hall resistivity demonstrates that irradiation leaves carrier densities unchanged and merely reduces mobility. This is consistent with an increase in the nonmagnetic scattering rate τ^{-1} caused by the (expected) creation of pointlike Frenkel-pair defects. The superconducting transition temperature T_c decreases with increasing residual resistivity ρ_0. Specifically, it changes from $T_{c,0} = 1.76$ K in the pristine sample, where $\rho_0 = 0.6\ \mu\Omega$ cm, to $T_c(2.41\ \text{C/cm}^2) = 1.65$ K, where $\rho_0 = 2.3\ \mu\Omega$ cm. London penetration depth λ and thermal conductivity κ measurements show that the superconducting state remains fully gapped. Importantly, the temperature dependence of $\lambda(T)$ can be well described by a *single*-gap energy scale.

A. Suppression of T_c with irradiation dose

A measurement of the rate of T_c suppression with increasing levels of nonmagnetic disorder can be used to distinguish different superconducting pairing states (see, e.g., [40,50,64,65]). To quantitatively analyze the suppression of T_c with irradiation dose, we plot in Fig. 6 the transition temperature ratio $T_c/T_{c,0}$ as a function of the experimentally determined dimensionless scattering parameter [64] (see also Appendix D)

$$\gamma^\lambda = \frac{\hbar}{2\pi k_B \mu_0}\frac{\Delta\rho_0}{\lambda_0^2 T_{c,0}} = 0.98\frac{\Delta\rho_0\ (\mu\Omega\,\text{cm})}{\lambda_0^2\ (10^{-7}\ \text{m})T_{c,0}\ (\text{K})}. \quad (2)$$

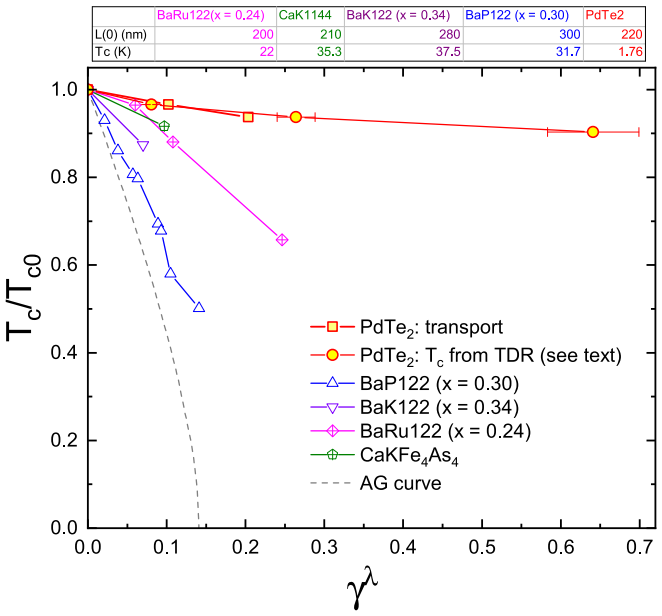

FIG. 6. T_c suppression rate upon electron irradiation in $PdTe_2$ in comparison with several representative cases. The temperature axis is normalized by T_{c0} in the pristine state, and the scattering rate γ^λ is calculated from Eq. (2). For comparison, reports on other materials are plotted together: BaRu122 ($x = 0.24$) [64], CaK1144 [15], BaK122 ($x = 0.34$) [66], and BaP122 ($x = 0.3$) [67].

Here, $\Delta\rho_0$ is the residual resistivity change due to electron irradiation, and λ_0 is the zero-temperature penetration depth. The numerical prefactor 0.98 emerges when using the units shown, i.e., expressing residual resistivity change $\Delta\rho_0$ in $\mu\Omega$ cm, λ_0 in 10^{-7} m and $T_{c,0}$ in K. In Fig. 6, there are two different sets of $PdTe_2$ data: one from transport (Fig. 1) and the other from TDR (Fig. 4), respectively. For TDR data, we do not have corresponding resistivity values. So, we used the slope in Fig. 1(c), and we converted the dose to $\Delta\rho_0$. Then, this $\Delta\rho_0$ is used to calculate γ^λ. Both curves of $PdTe_2$ are consistent with each other.

We extract important information about the superconducting state from the observed (initial) slope of the T_c suppression. The upper limit (i.e., fastest) suppression is the well-known AG law [22]: $\delta T_c/T_{c,0} = -\frac{\pi^2}{2}\gamma^\lambda$ (dashed line in Fig. 6). This occurs when all scattering processes are pair breaking, which is, for example, the case for TRA scattering off magnetic impurities in an isotropic, single-band spin-singlet superconductor. The lower limit corresponds to the Anderson theorem, which is the case in which T_c is completely unaffected by scattering, $\delta T_c/T_{c,0} = 0$ [23–25]. This occurs, for example, for TRS scattering off nonmagnetic impurities in the isotropic single-band s-wave case. The phenomenology becomes richer in the presence of spatial anisotropies of the gap and multiple orbitals or bands [28–34,44,45]. We have therefore included the experimentally observed T_c suppression upon electron irradiation in various iron-based superconductors $Ba(Fe_{1-x}Ru_x)_2As_2$ ($x = 0.24$) [64], $CaKFe_4As_4$ [15], $(Ba_{1-x}K_x)Fe_2As_2$ ($x = 0.34$) [66], and $BaFe_2(As_{1-x}P_x)_2$ ($x = 0.3$) [67].

Below, we discuss in detail under which conditions the different potential pairing states in $PdTe_2$ could give rise to the observed finite suppression rate. Comparison with other experimental observations will then be used to rule out (or at least disfavor) certain states. For example, the fact that $\lambda(T)$ is well described by a single-gap energy scale limits the degree of possible gap anisotropy in the system.

To analyze the different pairing scenarios, we make use of a generalized Anderson theorem that was recently derived by one of us [45]. The theorem is stated in terms of (anti)commutators of the superconducting order parameter, the disorder potential, and the Hamiltonian in the normal state. We show below that the rate of T_c suppression is determined by the value of these (anti)commutators, averaged over the Fermi surface. As a result, the suppression rate is small if the (anti)commutators are only weakly violated on average.

In the following, we describe the possible superconducting pairing states and their topology, before deriving the conditions under which their respective superconducting T_c would be suppressed with the experimentally observed rate.

B. Candidate pairing states

As analyzed in detail in our previous work [8], the point group D_{3d} and Fermi surface topology of $PdTe_2$ allow for only three distinct pairing symmetries with a full superconducting gap that are, hence, consistent with our penetration depth and thermal transport data: the topologically trivial s-wave, spin-singlet superconductor transforming under the irreducible representation (IR) A_{1g} and the two p-wave triplet states, A_{1u} and $E_u(1,0)$. The latter two triplet states *can* be topologically nontrivial depending on microscopic details (see below). As the $E_u(1,0)$ state breaks rotational symmetry, its gap is in general anisotropic. As such, the exponential behavior of $\lambda(T)$ observed at all temperatures requires fine-tuning for the $E_u(1,0)$ state. Therefore, we will mostly focus on the A_{1g} and A_{1u} states in the following discussion.

In any system, such as $PdTe_2$, with both time-reversal, Θ, and inversion, P, symmetries, all bands have to be doubly degenerate and one can introduce a *pseudospin basis* at each $\boldsymbol{k}$-point with the same transformation properties as the electron's spin. As will become important below, the associated basis states are in general complicated, $\boldsymbol{k}$-dependent admixtures of spin and orbital degrees of freedom in a spin-orbit-coupled multiorbital system such as $PdTe_2$. Denoting the Pauli matrices in pseudospin space by σ_j, $j = 1, 2, 3$, the corresponding order parameters can be written as

$$\Delta_{\boldsymbol{k}} = \Delta_0(\boldsymbol{k}) i\sigma_2 \tag{3}$$

for the A_{1g} state, and

$$\Delta_{\boldsymbol{k}} = \sum_{j=1}^{3} (\boldsymbol{d}_{\boldsymbol{k}})_j \sigma_j i\sigma_2 \tag{4}$$

with $\boldsymbol{d}_{\boldsymbol{k}} = d_0(X_{\boldsymbol{k}}, Y_{\boldsymbol{k}}, Z_{\boldsymbol{k}})$ for the A_{1u} state [8]. Here $\Delta_0(\boldsymbol{k})$ transforms as a scalar under all symmetry operations g of the point group D_{3d}, $\Delta_0(g\boldsymbol{k}) = \Delta_0(\boldsymbol{k})$, and $X_{\boldsymbol{k}}$, $Y_{\boldsymbol{k}}$, and $Z_{\boldsymbol{k}}$ transform as k_x, k_y, and k_z under D_{3d}. Motivated by the experimental observation of a fully established gap, we assume (unless stated otherwise) an absence of accidental nodes, $\Delta_0(\boldsymbol{k})$, $|\boldsymbol{d}_{\boldsymbol{k}}| \neq 0$ for $\boldsymbol{k}$ in the vicinity of a Fermi surface of the system.

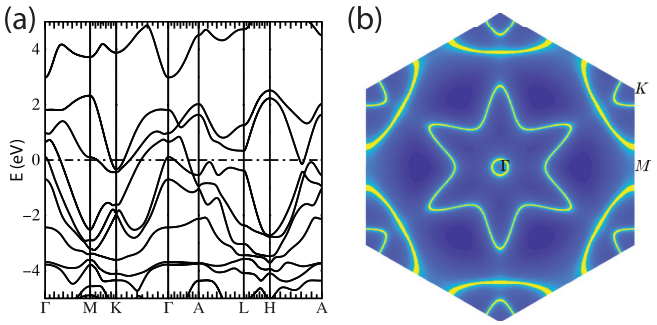

FIG. 7. (a) Band structure of $PdTe_2$. The horizontal dot-dashed line indicates the Fermi level. (b) Fermi surface contour in $PdTe_2$ for the $k_z = 0$ (Γ-M-K) plane.

According to band-structure calculations and experiment [4,5], the system has several Fermi surfaces. This is confirmed by our DFT calculations using a full-potential linear augmented plane wave (FP-LAPW) method, as implemented in WIEN2K [68] (for details on DFT, see Appendix E). As shown in Fig. 7, there are two hole pockets enclosing the Γ point, both of which arise from bands associated with the type-II Dirac cone below the Fermi level, and additional Fermi surfaces around the K and K' points. To specify the pairing states, let us first neglect the pockets around K and K', which will later be taken into account when discussing the impact of disorder whenever relevant. With two Fermi surfaces, we have to distinguish between superconducting states that have the same sign (denoted by the superscript "++" in the following) and have opposite sign (superscript "+−") on the two Fermi surfaces. We thus have four different states, A_{1g}^{++}, A_{1g}^{+-}, A_{1u}^{++}, and A_{1u}^{+-}. The two singlet states A_{1g}^{++} and A_{1g}^{+-} have exactly the same transformation properties under all symmetries of the system, however they require different interactions driving the superconducting instability: the A_{1g}^{++} state is expected to arise if the electron-phonon coupling (conventional pairing mechanism) or fluctuations of a time-reversal-symmetric collective electronic mode (such as charge-density fluctuations) provide the pairing glue [69]. Stabilizing the A_{1g}^{+-} phase requires an effectively repulsive interaction between states on the two Fermi surfaces. As we will discuss below, also the behavior in the presence of disorder is different for these two singlet states. The two triplet states, A_{1u}^{++} and A_{1u}^{+-}, also share the same symmetry properties and are expected to require repulsive intra-Fermi-surface interactions. Which of the two is realized depends on the sign of the interactions between the two bands.

C. Chiral basis and topology

Let us now determine the topological properties of the four pairing states, A_{1g}^{++}, A_{1g}^{+-}, A_{1u}^{++}, and A_{1u}^{+-}, and analyze which types of scattering processes are detrimental to superconductivity. For this, we will employ the following "chiral" basis: let $\boldsymbol{k}$ be in the vicinity of one of the doubly degenerate Fermi surfaces of the system. We label the ones around the Γ point as $n = 1, 2$ in the following (see Fig. 7). As a result of $P\Theta$ symmetry, the corresponding Bloch Hamiltonian will just be

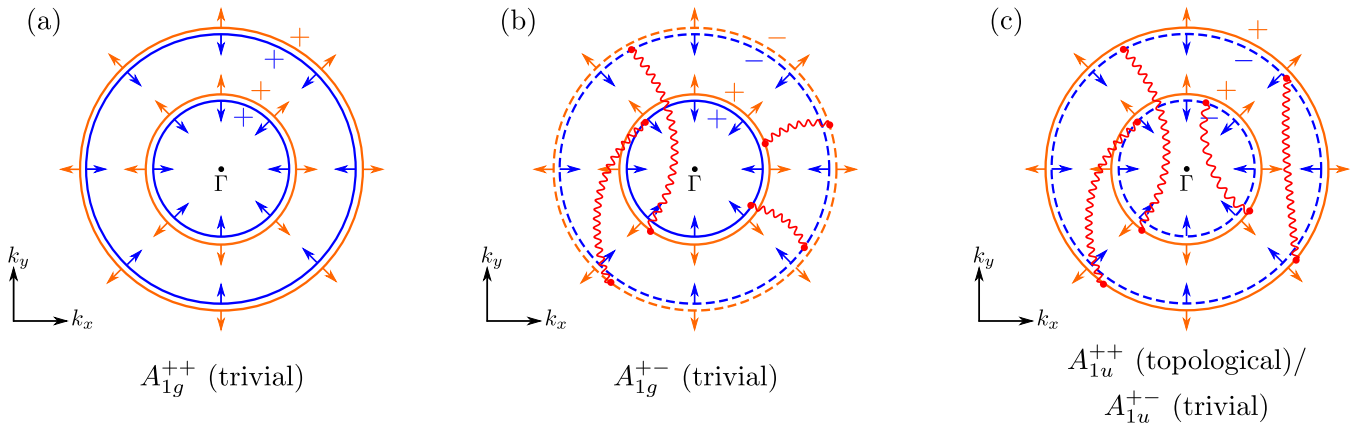

FIG. 8. Illustration of the superconducting order parameter on the different Fermi surfaces around the Γ point with solid (dashed) lines referring to positive (negative) sign of $\Delta_s(\boldsymbol{k})$ [see Eq. (6)] and using the pseudospin-triplet basis defined in the main text; see Eq. (5). The arrows indicate the corresponding pseudospin polarizations taking the simplest form of the triplet vector, $\boldsymbol{d}_{\boldsymbol{k}} \propto (k_x, k_y, k_z)^T$, as an example. For clarity of the figure, we only show a two-dimensional cut in three-dimensional momentum space. While the system also has further Fermi surfaces around the K and K' points, we focus here on those around the Γ point as the extension to additional Fermi surfaces is straightforward and will be discussed later. We distinguish between candidate pairing states transforming under A_{1g} with (a) equal (A_{1g}^{++}) and (b) opposite (A_{1g}^{+-}) sign of the singlet order parameter on the Fermi surfaces and (c) transforming under A_{1u}. While the singlet states are topologically trivial, the triplet state can be nontrivial, depending on the relation between the triplet vectors on the two Fermi surfaces. In the limit where the gap magnitude is isotropic and focusing on nonmagnetic impurities, only scattering processes between the Fermi surfaces that are connected by red wiggly lines are pair-breaking. The absence of wiggly lines in (a) indicates that the state A_{1g}^{++} with a constant gap is protected against all types of scattering processes, reproducing the Anderson theorem [23–25].

diagonal in pseudospin space, $h_{\boldsymbol{k}} = \sigma_0 \epsilon_{\boldsymbol{k}n}$ with band energy $\epsilon_{\boldsymbol{k}n}$. Instead of choosing pseudospin up and down as basis states, we will take the nondegenerate eigenstates $|\phi_{\boldsymbol{k}}^s\rangle$, $s = \pm$, of the infinitesimally perturbed Hamiltonian

$$h'_{\boldsymbol{k}} = \sigma_0 \epsilon_{\boldsymbol{k}n} + \alpha\, \boldsymbol{d}_{\boldsymbol{k}} \cdot \boldsymbol{\sigma}, \quad \alpha \to 0^+, \tag{5}$$

satisfying $h'_{\boldsymbol{k}} |\phi_{\boldsymbol{k}}^s\rangle = (\epsilon_{\boldsymbol{k}n} + s\, 0^+) |\phi_{\boldsymbol{k}}^s\rangle$. Since the triplet vector obeys $\boldsymbol{d}_{\boldsymbol{k}} = -\boldsymbol{d}_{-\boldsymbol{k}} \in \mathbb{R}^3 \setminus \{0\}$, the extra term in Eq. (5) lifts the degeneracy by infinitesimally breaking inversion while preserving time-reversal symmetry; it therefore holds that $\Theta |\phi_{\boldsymbol{k}}^s\rangle \propto |\phi_{-\boldsymbol{k}}^s\rangle$ and $P |\phi_{\boldsymbol{k}}^s\rangle \propto |\phi_{-\boldsymbol{k}}^{-s}\rangle$, where we suppressed momentum-dependent phase factors. Being infinitesimal, the second term in Eq. (5) has no physical consequences and should be viewed as a bookkeeping tool that allows us to define a convenient basis, $\{|\phi_{\boldsymbol{k}}^+\rangle, |\phi_{\boldsymbol{k}}^-\rangle\}$. We will refer to this "chiral" basis as the *pseudospin-triplet basis*.

It is easy to see that the superconducting order parameters represented in this basis have the form ($s, s' = \pm$)

$$\widetilde{\Delta}_{ss'}(\boldsymbol{k}) = \langle \phi_{\boldsymbol{k}}^{s'} | \Delta_{\boldsymbol{k}} (i\sigma_2)^\dagger | \phi_{\boldsymbol{k}}^s \rangle = \delta_{s,s'} \Delta_s(\boldsymbol{k}) \tag{6}$$

with $\Delta_s(\boldsymbol{k}) = \Delta_0(\boldsymbol{k})$ for the singlet state transforming under A_{1g} and $\Delta_s(\boldsymbol{k}) = s|\boldsymbol{d}_{\boldsymbol{k}}|$ for the triplet A_{1u}. Taking a finite value of α to make the different basis states $s = +$ (orange) and $s = -$ (blue) discernible, we show in Fig. 8 a two-dimensional schematic cut of the Fermi surfaces around the Γ point; furthermore, the sign of $\Delta_s(\boldsymbol{k})$ is indicated (solid/dashed lines) for the different candidate pairing states. Note that $\Delta_s(\boldsymbol{k}) \in \mathbb{R}$ (without loss of generality) due to time-reversal symmetry and that $\Delta_s(\boldsymbol{k})$ has a fixed sign on each Fermi surface since we focus on fully gapped superconducting states without accidental nodes.

In addition to providing a convenient way of illustrating the pairing states, the pseudospin-triplet basis also allows us to easily infer their topological features: since all candidate states preserve Θ, we have to view the superconductors as members of class DIII. Due to the infinitesimal perturbation in Eq. (5), the Fermi surfaces are singly degenerate and the expression for the corresponding $\mathbb{Z}$-valued topological invariant ν derived in Ref. [70] can be applied. Using the result [69] that the Chern numbers of the two (infinitesimally split) Fermi surfaces of the Hamiltonian in Eq. (5) must be opposite, one can write

$$\nu = \sum_n C_n^+ \frac{\mathrm{sgn}(\Delta_+(\boldsymbol{k}_n)) - \mathrm{sgn}(\Delta_-(\boldsymbol{k}_n))}{2}. \tag{7}$$

In Eq. (7), the summation over n involves all pairs of infinitesimally split Fermi surfaces (in Fig. 8, there are two such pairs, $n = 1, 2$, of Fermi surfaces enclosing the Γ point, i.e., pairs of orange and blue circles), C_n^+ is the Fermi surface Chern number of the $s = +$ member of the pair n, and $\boldsymbol{k}_n$ is an arbitrary momentum point on Fermi surface n.

Recalling that we have $\Delta_+(\boldsymbol{k}) = \Delta_-(\boldsymbol{k})$ for the singlet states, we immediately find $\nu = 0$ from Eq. (7). Consequently, both A_{1g}^{++} and A_{1g}^{+-} are topologically trivial. This is different for the triplet states for which we have $\Delta_+(\boldsymbol{k}) = -\Delta_-(\boldsymbol{k}) \in \mathbb{R}^+$ and, thus, $\nu = \sum_n C_n^+$. As each Fermi surface encloses an odd number of time-reversal invariant momenta (only the Γ point), it follows that C_n^+ has to be odd [70] and, as such, nonzero. To illustrate this with a specific example, assume that $\boldsymbol{d}_{\boldsymbol{k}} \sim f(|\boldsymbol{k}|)(k_x, k_y, k_z)^T$ with some real-valued function f describing the radial dependence of the triplet vector. If $f(|\boldsymbol{k}|)$ has the same sign on both Fermi surfaces, we find $C_1^+ = C_2^+ = 1$ and the topologically nontrivial value $\nu = 2$; this is the A_{1u}^{++} state (which we define more generally by $C_1^+ \neq -C_2^+$). In the case of the A_{1u}^{+-} state, $f(|\boldsymbol{k}|)$ changes sign leading to $C_1^+ = -C_2^+ = 1$ and $\nu = 0$ (topologically trivial).

To summarize, the singlets A_{1g}^{++}, A_{1g}^{+-} are topologically trivial. The triplet states can be topologically nontrivial with

a nonzero, even value of the invariant ν in Eq. (7) depending on the form of the $\boldsymbol{d}_{\boldsymbol{k}}$ vector: for instance, if $\boldsymbol{d}_{\boldsymbol{k}} \sim f(|\boldsymbol{k}|)(k_x, k_y, k_z)^T$, the state will be topological (trivial) if f does not change sign, corresponding to A_{1u}^{++} (corresponding to A_{1u}^{+-} when changing sign) between the two Fermi surfaces around the Γ point.

D. Generalized Anderson theorem

To discuss the expected impact of impurity scattering for the different candidate pairing states, we use the *generalized Anderson theorem* of Ref. [45]: let $\hat{W}$ be the matrix comprising the impurity-induced scattering amplitudes $(\hat{W})_{\boldsymbol{k}\alpha,\boldsymbol{k}'\alpha'} = \langle \boldsymbol{k}\alpha|W|\boldsymbol{k}'\alpha'\rangle$ between the single-particle states $|\boldsymbol{k}\alpha\rangle$ and $|\boldsymbol{k}'\alpha'\rangle$ of the clean normal-state Hamiltonian $(h_{\boldsymbol{k}})_{\alpha\alpha'}$ for which crystal momentum $\boldsymbol{k}$ is still a good quantum number. Here, α and α' label all remaining relevant degrees of freedom, such as spin and various orbitals. Similarly, we introduce the matrix elements $\hat{D}_{\boldsymbol{k}\alpha,\boldsymbol{k}'\alpha'} = \delta_{\boldsymbol{k},\boldsymbol{k}'} \langle \boldsymbol{k}\alpha|\Delta_{\boldsymbol{k}} T^\dagger|\boldsymbol{k}'\alpha'\rangle$ of the pairing order parameter $\Delta_{\boldsymbol{k}}$, where T is the unitary part of the time-reversal operator, $\Theta = T\mathcal{K}$ ($\mathcal{K}$ denotes complex conjugation); for instance, we have $T = i\sigma_2$ in the (pseudo)spin basis described above. As long as the electronic states are still delocalized in the vicinity of the Fermi ($k_F\ell \gg 1$), the superconducting critical temperature is unaffected by the presence of disorder if both

$$[\hat{h}, \hat{D}]_- = 0, \tag{8a}$$

where $\hat{h}_{\boldsymbol{k}\alpha,\boldsymbol{k}'\alpha'} = \delta_{\boldsymbol{k},\boldsymbol{k}'}(h_{\boldsymbol{k}})_{\alpha\alpha'}$, and

$$[\hat{W}, \hat{D}]_{-t_W} = 0 \tag{8b}$$

hold. Here $[\hat{A}, \hat{B}]_\pm = \hat{A}\hat{B} \pm \hat{B}\hat{A}$ and $t_W = +$ ($t_W = -$) for nonmagnetic (magnetic) disorder, i.e., $\Theta W \Theta^\dagger = t_w W$. While this general form of Anderson's theorem has been derived in Ref. [45], we present a compact justification in Appendix A for convenience and to provide a more formal definition of the notation used. We emphasize that this result holds for arbitrary momentum dependence of the order parameter. One advantage of the condition (8) for the validity of the generalized Anderson theorem is that it only depends on the (anti)commutation relations of the order parameter, the normal-state Hamiltonian, and the disorder potential, and hence it can be readily tested in any single-particle basis.

The pseudospin triplet basis introduced above is most convenient for us. In this low-energy description, only the matrix elements of the superconducting order parameter within each band (associated with the Fermi surfaces $n = 1, 2$ or $n = 1, 2, 3, 4$ depending on whether we neglect or take into account the Fermi surfaces around the K, K' points) are kept, and hence Eq. (8a) is automatically satisfied. Using the form in Eq. (6) of the matrix elements of the superconducting order parameter in the pseudospin-triplet basis, the remaining second condition (8b) simply becomes

$$C_{\boldsymbol{k}s,\boldsymbol{k}'s'} = 0, \quad \forall\, \boldsymbol{k}, \boldsymbol{k}', s, s', \tag{9a}$$

where we introduced (no summation over repeated indices)

$$C_{\boldsymbol{k}s,\boldsymbol{k}'s'} := [\Delta_s(\boldsymbol{k}) - t_W \Delta_{s'}(\boldsymbol{k}')] \langle \phi_{\boldsymbol{k}}^s | W | \phi_{\boldsymbol{k}'}^{s'} \rangle. \tag{9b}$$

This means that the superconducting state is protected against nonmagnetic (magnetic) disorder if scattering matrix elements are nonzero only between single-particle states $|\phi_{\boldsymbol{k}}^s\rangle$ and $|\phi_{\boldsymbol{k}'}^{s'}\rangle$ for which the superconducting order parameter $\Delta_s(\boldsymbol{k})$ has the same value (same magnitude but opposite sign). Therefore, we can readily read off which scattering events are pair breaking for the different superconducting states in Fig. 8.

The impurities induced by electron irradiation are nonmagnetic, and we thus focus on $t_W = +$ in the following. Let us first discuss the case of a single, isotropic gap energy scale, i.e., that $\Delta_s(\boldsymbol{k})$ only depends on s and the Fermi surface where $\boldsymbol{k}$ is located and that the magnitude $|\Delta_s(\boldsymbol{k})|$ is constant; we will examine the general case below. The order parameter is then identical on all Fermi surfaces for the A_{1g}^{++} state. As we read off from Eq. (9), its critical temperature will be unaffected by any time-reversal-symmetric (TRS) impurity as long as the mean free path is much larger than the Fermi wavelength $k_F\ell \gg 1$ (no localization). This reproduces the well-known conventional Anderson theorem for a multiband system [23–25]. This is different for the A_{1g}^{+-} state, which is prone to scattering between the small and large pockets as a consequence of the sign change of $\Delta_s(\boldsymbol{k})$ between the two Fermi surfaces [see Fig. 8(b)]. Similarly, both triplet states A_{1u}^{++} and A_{1u}^{+-} are suppressed by scattering events between four out of the ten pairs of Fermi surfaces [see Fig. 8(c)].

E. Rate of T_c suppression

Let us now show that the commutator $C_{\boldsymbol{k}s,\boldsymbol{k}'s'}$ introduced in Eq. (9b) determines the rate of suppression of T_c with increasing scattering rate. As shown in detail in Appendix B, the change $\delta T_c := T_c - T_{c,0}$ of the critical temperature T_c relative to its clean value, $T_{c,0}$, can be expressed entirely in terms of $C_{\boldsymbol{k}s,\boldsymbol{k}'s'}$ as

$$\delta T_c/T_{c,0} \sim -\frac{\pi}{4T_{c,0}} \tau^{-1}\, \zeta \tag{10a}$$

in the asymptotic limit of low disorder configurations (small scattering rate $\tau^{-1} \to 0$). All nonuniversal features that depend, for instance, on details of the superconducting order parameter and impurity potential enter the dimensionless "sensitivity parameter"

$$\zeta = \frac{\sum_{\boldsymbol{k},\boldsymbol{k}'}^{\mathrm{FS}} \sum_{s,s'} |C_{\boldsymbol{k}s,\boldsymbol{k}'s'}|^2}{2\,\mathrm{tr}[W^\dagger W] \sum_{\boldsymbol{k}}^{\mathrm{FS}} \sum_s |\Delta_s(\boldsymbol{k})|^2}. \tag{10b}$$

The parameter ζ involves the Fermi surface average of the commutator in Eq. (9b). Here, we have written $\sum_{\boldsymbol{k}}^{\mathrm{FS}} \cdots \equiv \frac{1}{N_\Lambda} \sum_n \sum_{\boldsymbol{k},|\epsilon_{kn}|<\Lambda} \cdots$, with momentum cutoff Λ and total number of momentum points involved $N_\Lambda = \sum_{\boldsymbol{k}}^{\mathrm{FS}}$. The trace in the denominator is over all internal degrees of freedom (spin, orbitals) of the impurity potential to ensure proper normalization of ζ. Within our conventions, it holds that $\zeta = 1$ in the AG case, i.e., for magnetic impurities in a single-band, isotropic spin-singlet superconductor. We note that a special case (momentum-independent superconducting order parameter) of the observation that nonuniversal features can be absorbed into an effective scattering involving a commutator has been recently derived [71]; however, there are a few subtleties with the application of this commutator to be discussed below.

As follows from comparing the slopes in Fig. 6 of the AG law (black dashed line) and that of the curve measured for $PdTe_2$ (red solid line), we experimentally determine $\zeta \simeq 1/16$ for $PdTe_2$. This means that the suppression of T_c with disorder is weaker by approximately a factor of 16 compared to magnetic impurities in a superconductor with a momentum-independent order parameter on the Fermi surface. While $\zeta \simeq 1/16$ is small and one may naively conclude that the order must be A_{1g}^{++}, it is important to perform a quantitative analysis, taking the Fermi surface geometry properly into account. In the following, we therefore analyze in detail under which conditions the different fully gapped pairing options are consistent with the measured T_c suppression rate in $PdTe_2$.

F. Singlet pairing

Let us begin with singlet pairing and first note that we estimate $k_F\ell$ to be of order 10^3 based on our resistivity measurements (see Sec. III A). Due to the sizable value of $k_F\ell$, we expect localization effects to play only a minor role in the suppression of T_c in the three-dimensional system $PdTe_2$. In other words, a suppression of T_c with disorder can only be realized if the conditions of the generalized Anderson theorem in Eq. (9) are violated. The finite change of T_c with disorder that we observe is only consistent with either the A_{1g}^{+-} state or the A_{1g}^{++} superconductor with a momentum-dependent gap function $|\Delta_s(\boldsymbol{k})|$. In fact, we generically expect a momentum-dependent gap, however the observed temperature dependence of the London penetration depth is only consistent with moderately weak anisotropies of the gap function.

To evaluate the parameter ζ using Eq. (10b) for a specific pairing state such as singlet pairing, $\Delta_s(\boldsymbol{k}) = \Delta_0(\boldsymbol{k})$ with arbitrary momentum dependence, we need to make an assumption about the scattering matrix $\hat{W}$. Here, we consider the simplest case of $W = \sigma_0$, which corresponds to pointlike scalar disorder without any momentum dependence in the pseudospin basis. Note that this assumption on the impurity potential does not take into account the multiorbital nature of the system that might further suppress the impact of impurities on T_c [41–43], as we will discuss in Sec. IV G. Therefore, the following estimates on the momentum dependence and the degree of anisotropy of the order parameter $\Delta_0(\boldsymbol{k})$, which are based on the requirement to yield $\zeta \simeq 1/16$, should be viewed as lower bounds. From Eq. (10b), we find

$$\zeta = \frac{\langle|\Delta_0|^2\rangle_{\mathrm{FS}} - |\langle\Delta_0\rangle_{\mathrm{FS}}|^2}{2\langle|\Delta_0|^2\rangle_{\mathrm{FS}}}, \tag{11}$$

where $\langle\cdots\rangle_{\mathrm{FS}} \equiv \sum_{\boldsymbol{k}}^{\mathrm{FS}} \ldots$ denotes averaging over the Fermi surface. In accordance with previous results [32,34], the suppression of T_c can be expressed in terms of the variance of the gap on the Fermi surface.

Two possible types of anisotropy give rise to nonzero ζ in Eq. (11): (i) a variation of the order-parameter magnitude on the Fermi surfaces, and (ii) the order parameter is constant on each Fermi surface but has a different size on distinct Fermi surfaces. While both anisotropy types may be present simultaneously in the experimental system, we discuss them separately for clarity.

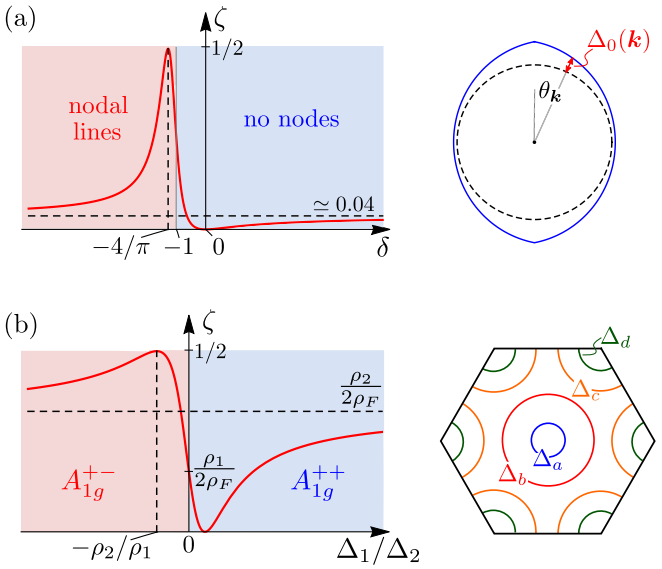

FIG. 9. Sensitivity ζ in Eq. (10) of singlet states with momentum-dependent order parameters to nonmagnetic disorder. In (a) we show ζ (left panel) for a singlet state with order parameter $\Delta_s(\boldsymbol{k}) = \Delta_0(\boldsymbol{k})$ varying on a single, spherical Fermi surface as parametrized in Eq. (12) and illustrated in the right panel. The sensitivity ζ of a state with a constant gap on each Fermi surface but two different values, Δ_n, of $\Delta_0(\boldsymbol{k})$ is shown in (b), left panel, as a function Δ_1/Δ_2 together with its dependence on the individual, ρ_n, and total, $\rho_F = \sum_n \rho_n$, density of states. Two relevant applications to the Fermi surfaces of $PdTe_2$, shown schematically in the right panel, are $\Delta_a = \Delta_b = \Delta_c = \Delta_1$, $\Delta_d = \Delta_2$, and $\Delta_a = \Delta_b = \Delta_1$, $\Delta_c = \Delta_2$. The former gives rise to an isotropic A_{1g}^{+-} state, the latter to an A_{1g}^{++} state with $\Delta_1/\Delta_2 = 2.1$, as discussed in the main text.

1. Anisotropic gap around the Fermi surface

In case (i), it is sufficient to focus on one Fermi surface around the Γ point that we assume to be spherical; its momenta satisfy $|\boldsymbol{k}| = k_F$. Let us for simplicity only take the leading order, i.e., lowest harmonic, momentum dependence of the order parameter into account:

$$\Delta_0(\boldsymbol{k}) = \Delta_0[1 + \delta\sin(\theta_{\boldsymbol{k}})], \tag{12}$$

where we have used spherical coordinates, $\boldsymbol{k} = k_F(\sin\theta_{\boldsymbol{k}}\cos\phi_{\boldsymbol{k}}, \sin\theta_{\boldsymbol{k}}\sin\phi_{\boldsymbol{k}}, \cos\theta_{\boldsymbol{k}})^T$, with the threefold rotation symmetry of the point group D_{3d} along the k_z axis. A single, dimensionless parameter $\delta \in \mathbb{R}$ parametrizes the gap variation; see the right panel in Fig. 9(a). Note that nodes are present if and only if $\delta \leqslant -1$. From Eq. (11), we obtain after straightforward algebra and converting all sums into integrals that the sensitivity parameter is given by

$$\zeta = \frac{(32 - 3\pi^2)\delta^2}{16(6 + 3\pi\delta + 4\delta^2)}. \tag{13}$$

This result is visualized in the left panel of Fig. 9(a). We first note that the maximal value of ζ that can be realized with positive δ is quite small and given by $1/2 - 3\pi^2/64 \simeq 0.037$. As follows from Eq. (12), large $\delta > 0$ means near nodes at the "poles" of the Fermi surface ($\theta_{\boldsymbol{k}} = 0$). Larger values of ζ occur for negative δ, which corresponds to having nodal lines ($\delta < -1$) or near-nodal lines ($-1 < \delta < 0$) in

the vicinity of the "equator" of the Fermi surface ($\theta_{\boldsymbol{k}} = \pi/2$). For our experimentally observed value of $\zeta \simeq 1/16$ in $PdTe_2$, there are two possible values $\delta \simeq -0.73$ or $\delta \simeq -5.02$ according to Eq. (13). While the latter corresponds to accidental nodal lines, the former has a nonzero gap on the entire Fermi surface but a significant degree of anisotropy with $\min_{\boldsymbol{k}} |\Delta_0(\boldsymbol{k})| / \max_{\boldsymbol{k}} |\Delta_0(\boldsymbol{k})| \simeq 0.27$. Both of these values of δ are not consistent with the measured temperature dependence of the penetration depth in Fig. 5, which can be well described by a single-gap energy scale and is known to exhibit a different temperature dependence in the presence of such significant gap anisotropy [17]. The variation of the magnitude of the order parameter on the Fermi surfaces seems unlikely to be the dominant source of the observed nonzero value of ζ.

2. Different constant gaps on multiple Fermi surfaces

Let us now focus on scenario (ii) where $\Delta_0(\boldsymbol{k})$ is constant on each Fermi surface, $n = 1, 2, \ldots, N$, but can take on different magnitudes on the different Fermi surfaces, i.e., $\Delta_0(\boldsymbol{k}_n) = \Delta_n$. Denoting the total density of states of the Fermi surface n by ρ_n, we immediately obtain from Eq. (11)

$$\zeta = \frac{1}{2}\left[1 - \frac{\left(\sum_n \rho_n \Delta_n\right)^2}{\left(\sum_n \rho_n \Delta_n^2\right)\sum_n \rho_n}\right]. \tag{14}$$

The behavior of ζ for the case of two Fermi sheets, $N = 2$, is shown in Fig. 9(b), left panel. Quantitative predictions require knowledge of the density of states ρ_n at the different Fermi surfaces. Using DFT calculations, we find for $PdTe_2$ that $\rho_a = 0.010\ \text{eV}^{-1}$, $\rho_b = 0.39\ \text{eV}^{-1}$, $\rho_c = 0.91\ \text{eV}^{-1}$, and $\rho_d = 0.045\ \text{eV}^{-1}$ [with labeling of Fermi surfaces shown in Fig. 9(b), right panel].

Let us for simplicity first concentrate on the case of only two different gap values Δ_1 and Δ_2. We consider the most general case with possibly four different gaps in Appendix F, and we show that this does not change our conclusions. For two gap sizes Δ_1, Δ_2 there are in total eight different possibilities of how these can be distributed over the four Fermi sheets a, b, c, d. The resulting gap ratios Δ_1/Δ_2 that are consistent with a T_c suppression slope of $\zeta = 1/16$ are listed in Appendix F. The most isotropic state we find is an A_{1g}^{+-} state with a sign change between the small electron pocket d and the other three pockets

$$\Delta_a = \Delta_b = \Delta_c = \Delta_2, \Delta_d = \Delta_1. \tag{15}$$

Such an isotropic state is a plausible option, since it is consistent with the observed isotropic temperature dependence of the penetration depth λ.

Interestingly, we find that the A_{1g}^{++} states always exhibit a larger degree of anisotropy. The smallest anisotropy we find is about $\Delta_1/\Delta_2 \simeq 2.1$ (2.0 when we allow for four different gap sizes). As shown in Appendix F, this occurs for a number of combinations of how the two gap sizes $\Delta_{1,2}$ are distributed over the four Fermi sheets. Importantly, such a large degree of anisotropy is expected to be visible in the temperature dependence of the London penetration depth that we find to be well described by a single-gap energy scale (see Sec. III) [17]. We conclude that the A_{1g}^{++} solutions are inconsistent with our observations of $\lambda(T)$ at least under the (natural) assumption that intra- and interband scattering is equally strong. We note that the observed slow (and seemingly saturating) T_c suppression at larger values of γ^{λ} (see Fig. 6), on the other hand, indicates extremely robust superconducting pairing. We suggest investigating this question further in future work.

To summarize, the most likely scenario in the A_{1g} channel is an unconventional A_{1g}^{+-} state with a sign change between the small electron pocket d around the K, K' points and the other Fermi sheets $\{a, b, c\}$. This state is completely isotropic with a ratio of gap magnitudes given by $|\Delta_1|/|\Delta_2| \simeq 1$. Any (conventional) A_{1g}^{++} pairing state has a significant degree of gap anisotropy. The minimal gap ratio we find is $\Delta_1/\Delta_2 \simeq 2$, making these states inconsistent with our observations of a London penetration depth $\lambda(T)$ that is well described by a single-gap energy scale.

G. Triplet pairing

In this subsection, we consider T_c suppression with disorder for the A_{1u} triplet state. From a direct comparison of the curve for $PdTe_2$ and that of the naive AG law in Fig. 6, one is tempted to conclude that the observed suppression of T_c in $PdTe_2$ is too weak to be consistent with a triplet pairing state. Indeed, as readily follows from Eq. (10), we obtain $\zeta = 1/2$ for any triplet state in the pseudospin approximation for the case of a single scattering rate arising from the most detrimental assumption of an impurity potential that is diagonal and momentum-independent in the pseudospin basis, $\langle \phi_{\boldsymbol{k}}^s | W | \phi_{\boldsymbol{k}'}^{s'} \rangle = W_0 \delta_{ss'}$. This applies to both the A_{1u} and also the third candidate pairing state $E_u(1, 0)$ [8] and agrees with previous results, e.g., Refs. [30,33]. Intuitively, $\zeta = 1/2$ results from the fact that only scattering processes *between* the infinitesimally split Fermi surfaces of $h_{\boldsymbol{k}}$ in Eq. (5) are pair-breaking, while also those *within* each of the Fermi surfaces are detrimental to superconductivity in the AG case (magnetic impurities and momentum-independent singlet superconductor); see Eq. (9b). To reconcile the observed suppression of T_c in $PdTe_2$ in Fig. 6 with a triplet pairing state, we therefore need approximately an additional factor of 8 of reduction of ζ.

As already alluded to above, such a reduction could in principle result from a suppression of the scattering matrix elements $\langle \phi_{\boldsymbol{k}}^s | W | \phi_{\boldsymbol{k}'}^{s'} \rangle$ that is related to the fact that we are working in the pseudospin basis. Consequently, even for the simplest case of $\boldsymbol{d}_{\boldsymbol{k}} \sim (k_x, k_y, k_z)$, the arrows in Fig. 8 refer to pseudospin polarizations rather than just spin polarizations. Due to the significant spin-orbit coupling, these will generally be momentum-dependent admixtures of spin and the Pd $4d$ and Te $5p$ orbitals relevant in the vicinity of the Fermi energy. This is confirmed within our detailed DFT calculations, which are presented in Appendix E. Such spin-orbital mixing is expected to suppress scattering, which can lead to a significant parametric enhancement [41–43] of the critical scattering strength relative to the naive AG law [22]. Intuitively, the reason for this suppression is that the angular dependence of the orbital and spin polarization of the Bloch states can lead to strongly suppressed matrix elements of the impurity potential, as has been discussed in detail in Ref. [43]. We note, however, that the required reduction in $PdTe_2$ is by a factor of 8, which is rather large. This makes the triplet state a rather unlikely candidate pairing state.

Nevertheless, it is worth emphasizing that under certain conditions a fully gapped spin-triplet SC can enjoy an Anderson theorem; for instance, this is possible if the order parameter is momentum-independent while its nontrivial symmetry properties are accounted for by its orbital structure. This was demonstrated by Michaeli and Fu in Ref. [41] by an explicit model calculation. This phenomenon can be readily understood from the generalized Anderson theorem (8), applied in the orbital basis: assuming that the impurity potential is trivial in orbital space, we have $\hat{W}_{\boldsymbol{k}\alpha,\boldsymbol{k}'\alpha'} = \delta_{\alpha,\alpha'} f_{\boldsymbol{k},\boldsymbol{k}'}$, which always commutes with a momentum-independent pairing potential, $\hat{D}_{\boldsymbol{k}\alpha,\boldsymbol{k}'\alpha'} = \delta_{\boldsymbol{k},\boldsymbol{k}'} D_{\alpha\alpha'}$. While Eq. (8b) is automatically satisfied, we have to keep in mind that also Eq. (8a) has to hold [81]. Therefore, the generalized Anderson theorem only applies if the normal-state Hamiltonian has additional symmetry, $[h_{\boldsymbol{k}}, D] = 0$. This is why Ref. [41] only finds a constant T_c in the presence of a chiral symmetry and agrees with the very recent result in Ref. [42].

We note in passing that a special case (the limit without momentum dependence of the order parameter) of the second condition (8b) has recently been rederived in Ref. [71]. In that work, however, the first condition (8a) was not properly taken into account. We believe that this is the reason why the results of Ref. [71] disagree with ours and those of Refs. [41,42]. In particular, the crucial first condition (8a) can generally be shown to be incompatible with the presence of nodes that are induced by the projection of a momentum-independent pairing potential on the Fermi surface. This contradicts the claim of a generalized Anderson theorem for nodal superconductors made in Ref. [71].

In contrast, the candidate A_{1u} triplet states in $PdTe_2$ possess a full gap and can thus, in principle, fulfill the first condition (8a) of the generalized Anderson theorem. Our observation that the rate of suppression of T_c with disorder is smaller than what we would expect from the AG law therefore does not necessarily rule out the triplet pairing state A_{1u}^{++}, or A_{1u}^{+-}, yet requires some fine-tuning of the microscopic orbital structure of the order parameter and the normal-state Hamiltonian. Depending on these microscopic details, spin-orbit coupling can be responsible for the additional suppression of the sensitivity parameter ζ by a factor of 8. Interestingly, our DFT results presented in Appendix E demonstrate that all four bands exhibit a substantial amount of mixing between states of opposite parity at the Fermi surface. This is a necessary (though not sufficient) condition for the protection mechanism outlined by Michaeli and Fu [41]. Further work, which takes microscopic details of the orbital content of the bands, possible pairing interactions, and the disorder potential into account, is necessary to investigate this intriguing possibility. Here we conclude that to explain the observed slow T_c suppression requires making more assumptions about microscopic details in case of the A_{1u} triplet states than for the A_{1g} singlet states. The triplet states are therefore less likely realized in $PdTe_2$.

V. CONCLUSIONS

We report on the impact of electron irradiation on the properties of the normal and superconducting state in $PdTe_2$. Our detailed study reveals that electron irradiation controllably tunes the nonmagnetic scattering rate τ^{-1} without affecting carrier densities. The superconducting state remains fully gapped under irradiation, but its transition temperature T_c is suppressed at a rate of about $\zeta \simeq 1/16$ compared to $\zeta = 1$ found for the Abrikosov-Gorkov law. We find the temperature dependence of the London penetration depth to be well described by a single gap energy scale, which is only consistent with a rather weak degree of anisotropy of the absolute value of the superconducting gap across the Fermi surfaces.

We use this information to infer properties of the superconducting pairing states, and in particular show under which conditions the different possible candidate states yield a T_c suppression rate consistent with experiment. One of our main conclusions is that the powerful probe of controlling the amount of disorder using electron irradiation must be combined with a thorough theoretical analysis in order to draw correct conclusions about the nature of the superconducting pairing state. Our analysis is based on the generalized Anderson theorem of Ref. [45] for multiband superconductors, which can be expressed in algebraic form in terms of (anti)commutators of the gap, the disorder potential, and the normal-state Hamiltonian. We use this powerful formulation to demonstrate that the suppression rate is governed by the Fermi surface average of the exact same commutator. Our general formulation agrees with previous results derived in various limits. A weak violation of the generalized Anderson theorem conditions therefore leads to a slow suppression rate. This situation can apply to both anisotropic spin-singlet superconductors as well as to (fully gapped) triplet paired states in the presence of strong spin-orbit coupling. Importantly, our concise formulation makes it easily applicable to other situations.

It is important to note that quantitative predictions of our theory depend on microscopic details such as the disorder potential matrix elements between different momenta and orbitals. Here, we focus on the (most agnostic) assumption of a momentum-independent disorder potential that acts diagonally in the pseudospin basis. For the A_{1g}^{+-} case, this corresponds to a ratio of inter- to intraband scattering rates equal to 1. The results also depend on the density of states at the different Fermi pockets, which we obtain using density functional theory.

Under these assumptions, we conclude that the most likely pairing state is the unconventional A_{1g}^{+-} state with a different sign of the gap on the inner hole pocket and the three other Fermi pockets. We find that such an A_{1g}^{+-} state can be completely isotropic, $|\Delta_1|/|\Delta_2 \simeq 1.0$, and can exhibit a T_c suppression with slope $\zeta = 1/16$ as we experimentally observe. In contrast, a conventional A_{1g}^{++} state must have a gap anisotropy of at least $\Delta_1/\Delta_2 \simeq 2$. This is not consistent with our results that $\lambda(T)$ can we well described by a single gap energy scale. We thus conclude that an anisotropic A_{1g}^{++} state is only consistent with the experimental data if the ratio of intra- to interband scattering is much smaller than 1. Further work should try to reveal details of the scattering defect potential introduced by electron irradiation, in particular its orbital structure.

ACKNOWLEDGMENTS

We thank Vladimir G. Kogan for illuminating discussion of generalized pair-breaking theories. We thank Morgan Masters, Joshua Slagle, and Victor Barrena Escolar for

support during the crystal growth. We also acknowledge discussions with D. C. Cavanagh and P. M. R. Brydon. The experimental work was supported by the U.S. Department of Energy (DOE), Office of Basic Energy Sciences, Division of Materials Sciences and Engineering. The experimental research was performed at Ames Laboratory. Ames Laboratory is operated for the U.S. DOE by Iowa State University under Contract No. DE-AC02-07CH11358. Development of a mobile thermal conductivity (MTC) setup was supported by the Laboratory Research and Development Program of The Ames Laboratory under the U.S. Department of Energy, Contract No. DE-AC02-07CH11358. N.H.J. was supported by the Gordon and Betty Moore Foundation's EPiQS Initiative (Grant No. GBMF4411). Irradiations realized on SIRIUS platform were supported by French National network of accelerators for irradiation and analysis of molecules and materials EMIR&A under project 18-5354. Y.L. and L.K. acknowledge the support from the U.S. DOE Early Career Research Program. M.S.S. acknowledges support from the German National Academy of Sciences Leopoldina through Grant No. LPDS 2016-12 and from the National Science Foundation under Grant No. DMR-1664842. P.P.O. acknowledges support from Iowa State University and Ames Laboratory Startup Funds.

APPENDIX A: GENERALIZED ANDERSON THEOREM

To be self-contained and to further clarify all quantities entering the generalized Anderson theorem used in the main text, we will provide a compact derivation of Eq. (8) in this Appendix. The following approach is adapted from [45], where also a diagrammatic proof can be found. We note that a special case of the following simplified argument has also been published in [44].

As opposed to the main text, we use second quantization with $c^\dagger_{\boldsymbol{k}\alpha}$ denoting the creation operator for an electron with momentum $\boldsymbol{k}$ and spin, orbital, etc. quantum numbers labeled by the multi-index α. We consider a general superconductor in d spatial dimensions with a mean-field Hamiltonian,

$$H_0 = \sum_{\boldsymbol{k}} c^\dagger_{\boldsymbol{k}\alpha}(h_{\boldsymbol{k}})_{\alpha\alpha'}c_{\boldsymbol{k}\alpha'} + \frac{1}{2}\sum_{\boldsymbol{k}}(c^\dagger_{\boldsymbol{k}\alpha}(\Delta_{\boldsymbol{k}})_{\alpha\alpha'}c^\dagger_{-\boldsymbol{k}\alpha'} + \text{H.c.}). \tag{A1}$$

As in the main text, $h_{\boldsymbol{k}}$ and $\Delta_{\boldsymbol{k}}$ are the normal-state Hamiltonian and superconducting order parameter matrix, respectively.

To probe the stability of the superconductor against impurity scattering, let us first consider a given disorder configuration,

$$\Delta H = \sum_{\boldsymbol{k},\boldsymbol{k}'} c^\dagger_{\boldsymbol{k}\alpha}\hat{W}_{\boldsymbol{k}\alpha,\boldsymbol{k}'\alpha'}c_{\boldsymbol{k}'\alpha'}, \tag{A2}$$

with $\hat{W}^\dagger = \hat{W}$ due to Hermiticity. As is well known, superconductivity behaves very differently in the presence of nonmagnetic (time-reversal even, $t_W = +$) and magnetic (time-reversal odd, $t_W = -$) disorder. Let us therefore split $\hat{W}$ into the respective components, $\hat{W} = \hat{W}^+ + \hat{W}^-$, with

$$\hat{W}^{t_W}_{\boldsymbol{k}\alpha,\boldsymbol{k}'\alpha'} = t_W\, T_{\alpha\beta}\big(\hat{W}^{t_W}_{-\boldsymbol{k}\beta,-\boldsymbol{k}'\beta'}\big)^* T^\dagger_{\beta'\alpha'}. \tag{A3}$$

Inspired by Anderson's work [23], we use a basis where Kramers partners, $c_{\boldsymbol{k}\alpha}$ and $T_{\alpha\beta}c^\dagger_{-\boldsymbol{k}\beta}$, are manifest: defining the Nambu spinor $\Phi_{\boldsymbol{k}\alpha} = (c_{\boldsymbol{k}\alpha}, T_{\alpha\beta}c^\dagger_{-\boldsymbol{k}\beta})^T$, the total Hamiltonian can be restated as $H_0 + \Delta H = \frac{1}{2}\sum_{\boldsymbol{k},\boldsymbol{k}'}\Phi^\dagger_{\boldsymbol{k}\alpha}(\hat{h}^{\text{BdG}})_{\boldsymbol{k}\alpha,\boldsymbol{k}'\alpha'}\Phi_{\boldsymbol{k}'\alpha'}$. We split it into three parts, $\hat{h}^{\text{BdG}} = \hat{h}^{\text{BdG}}_n + \hat{h}^{\text{BdG}}_\Delta + \hat{h}^{\text{BdG}}_W$, defined by

$$\hat{h}^{\text{BdG}}_n = \begin{pmatrix}\hat{h} & 0\\ 0 & -\hat{h}\end{pmatrix},\quad \hat{h}^{\text{BdG}}_\Delta = \begin{pmatrix}0 & \hat{\mathcal{D}}\\ \hat{\mathcal{D}}^\dagger & 0\end{pmatrix},\quad \hat{h}^{\text{BdG}}_W = \begin{pmatrix}\hat{W}^+ + \hat{W}^- & 0\\ 0 & -\hat{W}^+ + \hat{W}^-\end{pmatrix}, \tag{A4}$$

which correspond to the normal-state Hamiltonian, the superconducting pairing, and the disorder potential, respectively. Here we use the same conventions, $\hat{h}_{\boldsymbol{k}\alpha,\boldsymbol{k}'\alpha'} = \delta_{\boldsymbol{k},\boldsymbol{k}'}(h_{\boldsymbol{k}})_{\alpha\alpha'}$ and $(\hat{\mathcal{D}})_{\boldsymbol{k}\alpha,\boldsymbol{k}'\alpha'} = \delta_{\boldsymbol{k},\boldsymbol{k}'}(\Delta_{\boldsymbol{k}}T^\dagger)_{\alpha\alpha'}$, as in the main text.

It is not difficult to see that the gap of the system is not reduced by the presence of disorder, $\hat{W} \neq 0$, if

$$\big[\hat{h}^{\text{BdG}}_n + \hat{h}^{\text{BdG}}_W,\, \hat{h}^{\text{BdG}}_\Delta\big]_+ = 0, \tag{A5}$$

which indicates the stability of the superconductor against disorder. From Eq. (A4) it follows that $[\hat{h}^{\text{BdG}}_n,\, \hat{h}^{\text{BdG}}_\Delta]_+ = 0$ if the criterion in Eq. (8a) holds, i.e., if the normal-state Hamiltonian and the superconducting order parameter commute. In the eigenbasis of the normal-state Bloch Hamiltonian, this condition simply means

$$(E_{\boldsymbol{k}l} - E_{\boldsymbol{k}l'})\,\langle\psi_{\boldsymbol{k}l}|\Delta_{\boldsymbol{k}}T^\dagger|\psi_{\boldsymbol{k}l'}\rangle = 0, \tag{A6}$$

where $h_{\boldsymbol{k}}\,|\psi_{\boldsymbol{k}l}\rangle = E_{\boldsymbol{k}l}\,|\psi_{\boldsymbol{k}l}\rangle$; in other words, all matrix elements of the order parameter between different bands l and l' with $\delta^{ll'}_{\boldsymbol{k}} = |E_{\boldsymbol{k}l} - E_{\boldsymbol{k}l'}| \neq 0$ have to be zero. This is a very natural assumption as it typically holds that $|\Delta_{\boldsymbol{k}}| \ll \delta^{ll'}_{\boldsymbol{k}}$ in weak-coupling superconductors. However, in a generic basis, the condition Eq. (8a) has to be taken into account, as we discussed in the main text.

If $[\hat{h}^{\text{BdG}}_n,\, \hat{h}^{\text{BdG}}_\Delta]_+ = 0$ holds, Eq. (A5) becomes $[\hat{h}^{\text{BdG}}_W,\, \hat{h}^{\text{BdG}}_\Delta]_+ = 0$, which can be further simplified to

$$\sum_{t_W=\pm}[\hat{W}^{t_W}, \hat{D}]_{-t_W} = 0. \tag{A7}$$

Focusing on nonmagnetic and magnetic disorder separately, we have thus also recovered the second condition in Eq. (8).

We finally note that the same result can be obtained within the more conventional diagrammatic approach [72]: using the same low-energy description as in the main text where only states in the vicinity of the Fermi energy are included, it is shown in [45] that the superconducting critical temperature T_c is not affected by disorder in leading order in $(k_F l)^{-1}$ if Eq. (9a) is satisfied. Diagrammatically, this results from a cancellation of the disorder-induced self-energy and vertex correction. In the following Appendix, we will recover this cancellation to leading order in the impurity strength. We emphasize again that such a low-energy description implicitly assumes that the first condition (8a) or equivalently Eq. (A6), is satisfied.

APPENDIX B: LIMIT OF WEAK DISORDER

In this Appendix, we will follow the more conventional approach and consider an ensemble of disorder configurations; all physical quantities, such as the free energy below, will be averaged over disorder realizations. We take the disorder configurations to be Gaussian distributed with zero mean such that their probability distribution is uniquely defined by the correlator

$$\langle \hat{W}_{\boldsymbol{x}_1\alpha_1,\boldsymbol{x}_1'\alpha_1'}\hat{W}_{\boldsymbol{x}_2\alpha_2,\boldsymbol{x}_2'\alpha_2'}\rangle_{\rm dis} = \delta(\boldsymbol{x}_1-\boldsymbol{x}_1')\delta(\boldsymbol{x}_2-\boldsymbol{x}_2')\delta(\boldsymbol{x}_1-\boldsymbol{x}_2)\Gamma_{\alpha_1\alpha_1',\alpha_2\alpha_2'}. \tag{B1}$$

Here $W_{\boldsymbol{x}_1\alpha_1,\boldsymbol{x}_1'\alpha_1'}$ is the real-space representation of the disorder potential $\hat{W}$ in Eq. (A2), $\langle\cdots\rangle_{\rm dis}$ denotes the average over disorder configurations, and $\Gamma_{\alpha_1\alpha_1',\alpha_2\alpha_2'}$ encodes the orbital/spin structure of the impurities. In general, it can be expanded in Hermitian basis matrices $\{w_\mu\}$,

$$\Gamma_{\alpha_1\alpha_1',\alpha_2\alpha_2'} = \sum_{\mu,\mu'}\gamma_{\mu\mu'}(w_\mu)_{\alpha_1\alpha_1'}(w_{\mu'})_{\alpha_2\alpha_2'}, \tag{B2}$$

allowing for the presence of different types of impurities at the same time [43]. For notational simplicity, we will focus here on only one type of disorder at a time, $\Gamma_{\alpha_1\alpha_1',\alpha_2\alpha_2'} = \gamma(W)_{\alpha_1\alpha_1'}(W)_{\alpha_2\alpha_2'}$. We will not specify the orbital structure of W and only distinguish between time-reversal even ($t_W=+1$) and odd ($t_W=-1$) impurities, $\Theta W\Theta^\dagger = t_W W$. We normalize W such that $\sum_{\alpha_1,\alpha_2}|W_{\alpha_1\alpha_2}|^2 = 2$.

The general expression for the disorder-averaged free energy $\langle\mathcal{F}\rangle_{\rm dis}$ of [69] is also valid in the pseudospin-triplet basis of the main text. Assuming, as usual, that the superconducting order parameter only depends on the position (labeled by Ω in the following) on the Fermi surface, we write $\Delta_s(\boldsymbol{k}) \equiv \Delta_s(\Omega)$ and find to leading order in the superconducting order parameter

$$\langle\mathcal{F}\rangle_{\rm dis} \sim \sum_{s,s'}\int d\Omega\int d\Omega'\,\Delta_s^*(\Omega)D_{\Omega s,\Omega' s'}(T)\Delta_{s'}(\Omega'). \tag{B3}$$

The kernel is given by

$$D(T) = -T\sum_{\omega_n}[\mathcal{C}(\omega_n) - t_W\,\mathcal{S}^S b]^{-1} - \mathcal{V}^{-1}, \tag{B4}$$

where $\mathcal{S}_{\Omega s,\Omega' s'} = \mathcal{S}^0_{\Omega s,\Omega' s'} + \mathcal{S}^0_{\Omega s,\Omega_{\rm K}' s'}$ (here $\Omega_{\rm K}$ denotes the Kramers partner of Ω) and $\mathcal{S}^0_{\Omega s,\Omega' s'} = |\langle\phi^s_\Omega|W|\phi^{s'}_{\Omega'}\rangle|^2$ with the chiral states $|\phi^s_\Omega\rangle$ defined in Eq. (5). Furthermore, we have

$$\mathcal{C}_{\Omega s,\Omega' s'}(i\omega_n) = \frac{\delta_{s,s'}\delta_{\Omega,\Omega'}}{\rho_{\Omega s}}\left(\frac{|\omega_n|}{\pi} + \sum_{\tilde{s}}\int d\widetilde{\Omega}\,\rho_{\widetilde{\Omega}\tilde{s}}\,\mathcal{S}^S_{\Omega s,\widetilde{\Omega}\tilde{s}}\right), \tag{B5}$$

where $\rho_{\Omega s}$ is the angular-resolved density of states (within our current pseudospin approach with doubly degenerate Fermi surfaces, it holds that $\rho_{\Omega s} = \rho_\Omega$). Finally, the last term in Eq. (B4) is the inverse of the interaction kernel $\mathcal{V}_{\Omega s,\Omega' s'}$. While this term is crucial in determining the form of the superconducting order parameter, we will *assume* here that a certain order parameter is realized (requiring a certain underlying $\mathcal{V}$) and study the impact of disorder on it. For that reason, $\mathcal{V}$ will not explicitly appear in the results below.

In [45], it was shown that $\mathcal{S}$ cancels out entirely from Eq. (B4) if Eq. (9a) is satisfied. Here, we will focus on the leading-order impact of disorder for a general superconductor for which the left-hand side of Eq. (9a) is nonzero. Straightforward asymptotic analysis of Eq. (B3) yields

$$\frac{T_c}{T_{c,0}} = 1 - \frac{\pi^2}{2T_{c,0}}\rho_F\Gamma^{\rm eff} + O(\gamma^2), \tag{B6}$$

where T_c ($T_{c,0}$) is the critical temperature in the presence (absence) of disorder, ρ_F is the total density of states at the Fermi level, and the effective scattering rate

$$\rho_F\Gamma^{\rm eff} = \frac{\gamma}{4\sum_s\int d\Omega\,\rho_{\Omega s}|\Delta_s(\Omega)|^2}\sum_{s,s'}\int d\Omega\,d\Omega'\,\rho_{\Omega s}\rho_{\Omega' s'} \times\mathcal{S}^S_{\Omega s,\Omega' s'}[|\Delta_s(\Omega)|^2 - t_W\,\Delta_s^*(\Omega)\Delta_{s'}(\Omega')]. \tag{B7}$$

Using the property [73] $\Delta_s(\Omega) = \Delta_s(\Omega_{\rm K})$ that holds for any system with spinful time-reversal symmetry, $\Theta^2 = -\mathbb{1}$, and reexpressing the integrals in terms of momentum averages (N_Λ momentum points) over the states in the vicinity (cutoff Λ) of the Fermi energy,

$$\sum_{\boldsymbol{k}}^{\rm FS}\cdots := \frac{1}{N_\Lambda}\sum_n\sum_{\boldsymbol{k},|\epsilon_{\boldsymbol{k}n}|<\Lambda}\cdots, \tag{B8}$$

we can write

$$\Gamma^{\rm eff} \sim \gamma\frac{\sum^{\rm FS}_{\boldsymbol{k},\boldsymbol{k}'}\sum_{s,s'}|C_{\boldsymbol{k}s,\boldsymbol{k}'s'}|^2}{4\sum^{\rm FS}_{\boldsymbol{k}}\sum_s|\Delta_s(\boldsymbol{k})|^2}. \tag{B9}$$

Here $C_{\boldsymbol{k}s,\boldsymbol{k}'s'}$ is as defined in Eq. (9b) of the main text. Upon introducing the scattering rate $\tau^{-1} = 2\pi\rho_F\gamma$, we thus find Eq. (10) of the main text.

We point out that Eq. (B9) can also be written in the manifestly basis-independent form

$$\Gamma^{\rm eff} \sim \gamma\frac{\sum^{\rm FS}_{\boldsymbol{k},\boldsymbol{k}'}{\rm tr}[\hat{C}^\dagger_{\boldsymbol{k},\boldsymbol{k}'}\hat{C}_{\boldsymbol{k},\boldsymbol{k}'}]}{4\sum^{\rm FS}_{\boldsymbol{k}}{\rm tr}[\Delta^\dagger_{\boldsymbol{k}}\Delta_{\boldsymbol{k}}]}, \tag{B10}$$

where the trace is over pseudospin space and

$$\hat{C}_{\boldsymbol{k},\boldsymbol{k}'} = \Delta_{\boldsymbol{k}}T^\dagger W_{\boldsymbol{k},\boldsymbol{k}'} - t_W W_{\boldsymbol{k},\boldsymbol{k}'}\Delta_{\boldsymbol{k}'}T^\dagger; \tag{B11}$$

here all quantities are 2×2 matrices in pseudospin space.

Finally, note that we have chosen the normalization such that $\Gamma^{\rm eff} = \gamma$ in the case of spin-magnetic impurities in a singlet superconductor with a constant gap in a one-band model (only spin, no orbital).

APPENDIX C: TWO-BAND MODEL FIT TO LONGITUDINAL AND HALL RESISTIVITY

We fit the longitudinal and Hall resistivity ρ_{xx} and ρ_{xy} to the standard semiclassical expressions for a system with electron and hole charge carriers [52],

$$\rho_{xx} = \frac{1}{e_0}\frac{n_e\mu_e + n_h\mu_h + \mu_e\mu_h B^2(n_e\mu_h + n_h\mu_e)}{(n_e\mu_e + n_h\mu_h)^2 + \mu_e\mu_h B^2(n_e - n_h)^2}, \tag{C1}$$

$$\rho_{xy} = \frac{B}{e_0}\frac{n_h\mu_h^2 - n_e\mu_e^2 + (n_h - n_e)\mu_e^2\mu_h^2B^2}{(n_e\mu_e + n_h\mu_h)^2 + (n_e - n_h)^2\mu_e^2\mu_h^2B^2}. \tag{C2}$$

From the fit, we obtain the electron, n_e, and hole, n_h, charge-carrier densities as well as their respective mobilities

TABLE I. Parameters obtained from fitting longitudinal and Hall resistivity at $T = 5$ K to semiclassical two-band model expressions. For simplicity, the (inverse) scattering times are obtained under the assumption that $m^* = m_e$. For an effective mass different from the bare electron mass, they scale like $\tau_\alpha \to \tau_\alpha m_e/m^*$. Note that the mean free paths ℓ_α are independent of the effective masses.

Dose (C/cm^2)	n_e (m^{-3})	n_h (m^{-3})	μ_e (m^2/V s)	μ_h (m^2/V s)	τ_e^{-1} (meV)	τ_h^{-1} (meV)	ℓ_e (nm)	ℓ_h (nm)
0	$4.2(1) \times 10^{27}$	$2.2(1) \times 10^{27}$	0.10(1)	0.28(1)	70(2)	26(2)	344(5)	725(5)
1.33	$4.2(1) \times 10^{27}$	$2.2(1) \times 10^{27}$	0.05(1)	0.14(1)	140(2)	53(2)	172(5)	363(5)

μ_e and μ_h. This allows us to estimate the scattering rates τ_e^{-1}, τ_h^{-1} and the mean-free paths ℓ_e, ℓ_h in the system. All results from the two-band fit are collected in Table I.

APPENDIX D: DIMENSIONLESS SCATTERING RATE AND ABRIKOSOV-GORKOV LAW

Let us briefly describe our choice of using the dimensionless scattering rate

$$\gamma^\lambda = \frac{\hbar}{2\pi k_B \mu_0} \frac{\Delta\rho_0}{\lambda_0^2 T_{c,0}} = 0.97 \frac{\Delta\rho_0\ (\mu\Omega\,\mathrm{cm})}{\lambda_0^2\ (10^{-7}\ \mathrm{m}) T_{c,0}\ (\mathrm{K})} \tag{D1}$$

when comparing our experimental results of T_c suppression with the Abrikosov-Gorkov (AG) law (see Fig. 6). Here, $\Delta\rho_0 = \rho_0^{(\mathrm{irradiated})} - \rho_0^{(\mathrm{pristine})}$ denotes the change of the residual resistivity in the normal state induced by electron irradiation, $T_{c,0}$ is the transition temperature in the pristine sample, and λ_0 is the $T = 0$ London penetration depth in the pristine sample. We find $T_{c,0} = 1.76$ K and $\lambda_0 = 220$ nm for $PdTe_2$.

The AG law relates the suppression of T_c with the pair-breaking scattering rate τ_{pb} as

$$\frac{\delta T_c}{T_{c,0}} = -\frac{\pi}{4 T_{c,0} \tau_{\mathrm{pb}}}. \tag{D2}$$

For single-band, isotropic s-wave superconductors, τ_{pb} is given by the magnetic (spin-flip) scattering rate τ_m. Under the assumption that all scattering processes are pair-breaking, $\tau = \tau_{\mathrm{pb}}$, i.e., purely magnetic disorder in the isotropic single-band s-wave case, the AG law suppression corresponds to $\zeta = 1$ in Eq. (10a). In general, not all scattering processes that contribute to the residual normal-state resistivity $\rho_0 = m^*/(ne_0^2\tau)$ are pair breaking, which leads to $\zeta < 1$. For example, in the case of nonmagnetic (TRS) disorder, we have illustrated the pair-breaking processes for each of our candidate pairing states A_{1g}^{++}, A_{1g}^{+-}, A_{1u}^{++}, and A_{1u}^{+-} in Fig. 8.

We use electron irradiation to tune the scattering time τ by creating pointlike, nonmagnetic defects in the material. We have explicitly shown that electron irradiation only affects the scattering time τ and does not change the carrier density (see Sec. III and Table I). The change $\Delta\rho_0$ is thus directly proportional to $\Delta\tau^{-1}$, and thus

$$\gamma^\lambda = \frac{\hbar}{2\pi k_B \mu_0} \frac{\mu_0 n e_0^2}{m^*} \frac{m^*}{n e_0^2} \frac{\Delta\tau^{-1}}{T_{c,0}} = \frac{\hbar \Delta\tau^{-1}}{2\pi k_B T_{c,0}}, \tag{D3}$$

where we have used that the superfluid density equals the total carrier density at $T = 0$. We can thus express the AG law using the dimensionless scattering rate g_λ, which can be experimentally measured, in the form

$$\frac{\delta T_c}{T_{c,0}} = -\frac{\pi^2 g_\lambda}{2} \frac{\Delta\tau_{\mathrm{pb}}^{-1}}{\Delta\tau^{-1}}. \tag{D4}$$

By plotting our experimental results of $\delta T_c/T_{c,0}$ versus γ^λ, we can extract the dimensionless parameter $\zeta = \frac{\Delta\tau_{\mathrm{pb}}^{-1}}{\Delta\tau^{-1}}$ and compare with the AG law. The parameter ζ expresses the fraction of scattering processes that are pair-breaking. For example, $\zeta = 1$ for purely magnetic (TRA) scattering in an isotropic, single-band spin-single superconductor. In contrast, $\zeta = 1/2$ for nonmagnetic (TRS) disorder in the A_{1g}^{+-} state of a two-band superconductor with $\rho_1\Delta_1 = -\rho_2\Delta_2$ (see Fig. 9), assuming that the ratio of interband to intraband scattering is 1 (corresponding to orbitally insensitive disorder).

APPENDIX E: DENSITY FUNCTIONAL THEORY RESULTS

In this Appendix, we discuss additional *ab initio* results on the band structure, Fermi surface contour, and wave-function characters in $PdTe_2$. We also provide details on the density functional theory method we use.

1. Details of the DFT method

We perform calculations using our recently developed *ab initio* tight-binding (TB) framework [74]. Realistic TB Hamiltonians are constructed via the maximally localized Wannier functions (MLWFs) method [75] as implemented in WANNIER90 [76] through a postprocessing procedure [75,77,78] using the output of the self-consistent density functional theory (DFT) calculations. The details of our methods and applications can be found in Ref. [74].

DFT calculations are performed using a full-potential linear augmented plane wave (FP-LAPW) method, as implemented in WIEN2K [68]. The primitive cell contains one formula unit, and experimental lattice parameters [79] are adopted. The generalized gradient approximation of Perdew, Burke, and Ernzerhof [80] is used for the correlation and exchange potentials. To generate the self-consistent potential and charge, we employed $R_{\mathrm{MT}}K_{\max} = 8.0$ with muffin-tin (MT) radii $R_{\mathrm{MT}} = 2.5$ and 2.3 a.u., for Pd and Te, respectively. The calculations are performed with 1078 k-points in the irreducible Brillouin zone (BZ). They are iterated until charge differences between consecutive iterations are smaller than $1.0 \times 10^{-4}e$ and the total energy difference is lower than 0.01 mRy. Note that spin-orbit coupling is included in the Hamiltonian.

We construct the TB Hamiltonian by using 54 MLWFs, which correspond to s-, p-, and d-type orbitals for each of the three atoms in the unit cell. A real-space Hamiltonian $H(\mathbf{R})$ with dimensions 54×54 is constructed to accurately represent the band structures in the energy window of interest. We focus on six pairs of doubly degenerate bands around E_{F}

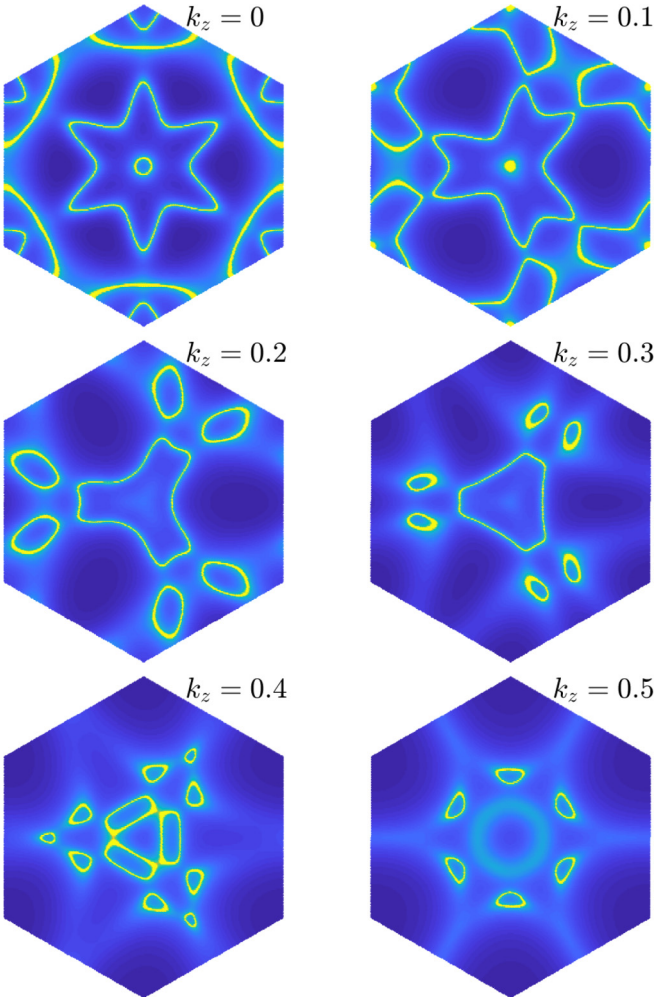

FIG. 10. Fermi surface contour in $PdTe_2$ for $k_z = 0, 0.1, 0.2, 0.3, 0.4, 0.5$.

and examine how their wave-function characters evolve along the k paths in the BZ.

2. Fermi surface

The band structure and a cross section of the Fermi surface in the k_x-k_y plane at $k_z = 0$ are shown in Fig. 7. We provide additional Fermi surface cross sections for other values of k_z in Fig. 10. The band structures are calculated in TB, within the energy window of interest, and they are essentially in perfect agreement with those obtained from DFT (not shown). There are four pairs of doubly degenerate bands across E_F on the Γ-M-K plane, forming two hole-pockets and two electron-pockets around Γ and K, respectively. The larger hole-pocket around Γ has a strong anisotropy so that the Γ-K direction has a much larger radius than the Γ-M direction.

3. Parity character of bands

We qualitatively estimate the parity mixing effects by calculating how the characters of bands near E_F change through the first BZ within TB. The **k**-point eigenvectors are calculated and projected on those of the Γ point, which

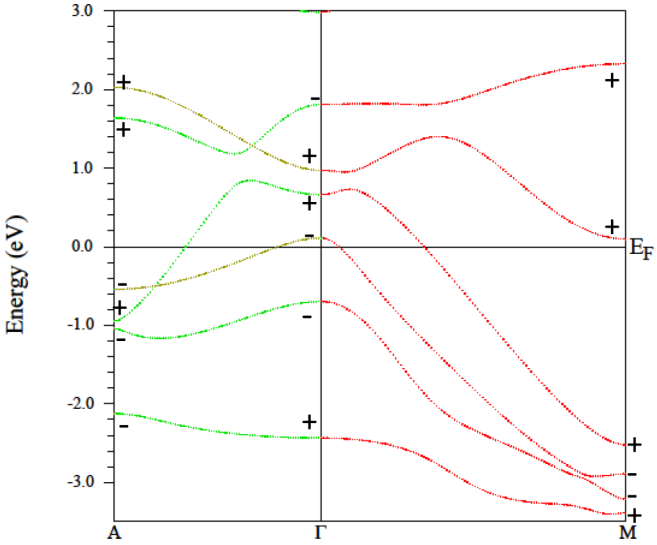

FIG. 11. Band structure along the A-Γ-M path in the Brillouin zone. The $\pm$ signs indicate the parity eigenvalues of the bands at the inversion symmetric high-symmetry points.

have a well-defined parity (see Fig. 11). Figure 12 shows the calculated projections.

The projection of the j_{th} pair at **k** on the i_{th} pair at Γ is defined as follows:

$$P(\Gamma, i; \mathbf{k}, j) = \sqrt{\left|\langle\psi_\Gamma^{i,1}|\psi_{\mathbf{k}}^{j,1}\rangle\right|^2 + \left|\langle\psi_\Gamma^{i,2}|\psi_{\mathbf{k}}^{j,1}\rangle\right|^2} + \sqrt{\left|\langle\psi_\Gamma^{i,1}|\psi_{\mathbf{k}}^{j,2}\rangle\right|^2 + \left|\langle\psi_\Gamma^{i,2}|\psi_{\mathbf{k}}^{j,2}\rangle\right|^2}. \quad \text{(E1)}$$

Here i and j denote the pair index of the six doubly degenerate bands near E_F, and $\psi_{\mathbf{k}}^{i,1}$ and $\psi_{\mathbf{k}}^{i,2}$ are the wave functions of the

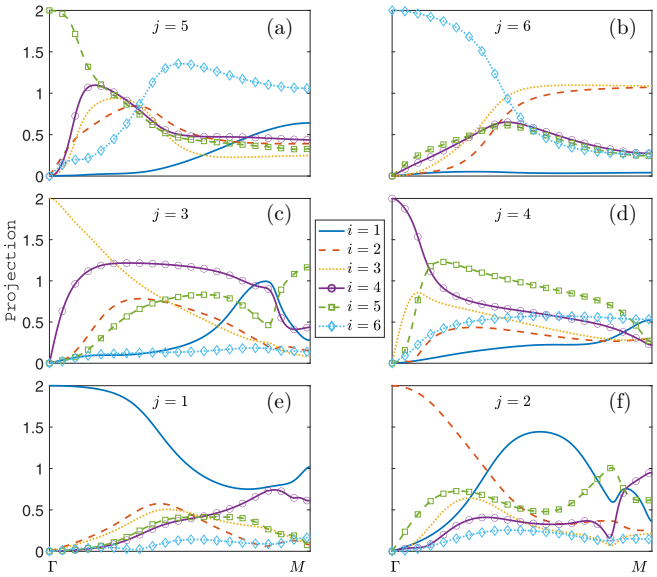

FIG. 12. Projections of the eigenstates at wave vector **k** along the Γ-M line on those of the Γ point, $P(\Gamma, i; \mathbf{k}, j)$. The index i or j denotes one of the six pairs of doubly degenerate bands near E_F, as shown in Figs. 7 and 11. The index $i, j = 1$ corresponds to the lowest energy band and $i, j = 6$ to the highest at Γ.

TABLE II. List of all possible gap anisotropies Δ_1/Δ_2 distributed over the four Fermi sheets of $PdTe_2$ $\{a, b, c, d\}$ that are consistent with the experimentally observed sensitivity parameter $\zeta \simeq 1/16$. The gap ratios are obtained from Eq. (14). The set C_1 denotes the Fermi sheets with gap Δ_1, the complementary set exhibits a gap of size Δ_2. The value $\nu = \sum_{n\in C_1}\rho_n/(\sum_n \rho_n - \sum_{n\in C_1}\rho_n)$ denotes the ratio of the density of states on the two pockets with either Δ_1 or Δ_2, where we obtain $\rho_a = 0.01$ eV^{-1}, $\rho_b = 0.39$ eV^{-1}, $\rho_c = 0.91$ eV^{-1}, and $\rho_d = 0.05$ eV^{-1} using DFT. We observe that the smallest anisotropy is obtained for the A_{1g}^{+-} state with $C_1 = \{d\}$ corresponding to a sign change between the small electron pocket d and the other three pockets. The minimal anisotropy for the A_{1g}^{++} is about 2.1 and is realized for various combinations $C_1 = (\{a, b\}, \{b\}, \{c\}, \{a, c\}, \{c, d\})$.

C_1	ν	$(\Delta_1/\Delta_2)_1$	$(\Delta_1/\Delta_2)_2$
$\{a\}$	7.5×10^{-3}	5.6	−3.3
$\{b\}$	0.40	2.1	0.32
$\{c\}$	2.1	2.8	0.48
$\{d\}$	0.034	3.3	−0.98
$\{a, b\}$	0.41	2.1	0.33
$\{a, c\}$	2.1	2.8	0.48
$\{a, d\}$	0.042	3.1	−0.78
$\{c, d\}$	2.4	3.0	0.47

two degenerate states of the corresponding i_{th} pair at wave vector $\mathbf{k}$.

APPENDIX F: GAP ANISOTROPIES CONSISTENT WITH T_c SUPPRESSION

In this Appendix, we provide details of the behavior of the sensitivity parameter ζ, which governs the T_c suppression rate, for the case of multiple constant gaps on different Fermi sheets. We analyze Eq. (14) in the case of $N = 2$ (one gap ratio) and $N = 4$ (three gap ratios).

1. Case of one gap ratio

Here we consider the case of two different gap sizes Δ_1 and Δ_2 in the system. The gaps are assumed to be constant around a given Fermi sheet. This corresponds to the $N = 2$ case in Eq. (14).

As shown in Fig. 7, the Fermi surface manifold of $PdTe_2$ consists of four Fermi sheets with the respective density of states

$$\rho_a = 0.01, \quad \rho_b = 0.39, \tag{F1}$$

$$\rho_c = 0.91, \quad \rho_d = 0.05. \tag{F2}$$

Let us denote the total Fermi surface manifold by $C = \{a, b, c, d\}$ and the subset that exhibits a gap Δ_1 by C_1. The remaining set $C_2 = C \setminus C_1$ correspond to the sheets with a gap Δ_2. In Table II, we present results of the gap anisotropies Δ_1/Δ_2 that are consistent with the experimentally observed sensitivity parameter $\zeta \simeq 1/16$. We consider all possible cases of how Δ_1 and Δ_2 are distributed over the four Fermi surfaces a, b, c, d. The table also contains the parameter ν that enters Eq. (14). This is the ratio between the combined densities of states of the bands C_1 and C_2:

$$\nu = \frac{\sum_{n\in C_1}\rho_n}{\sum_{n\in C_2}\rho_n}. \tag{F3}$$

As shown in Table II, the most isotropic state occurs for the A_{1g}^{+-} state with $C_1 = \{d\}$. For this state, the two gap sizes are about equal in magnitude, $|\Delta_1|/|\Delta_2| = 0.98$. This state is thus perfectly consistent with both the T_c suppression rate we observe and the fact that the London penetration depth can be well captured by a single gap energy scale.

The smallest anisotropy we find for the A_{1g}^{++} states is about 2: $\Delta_1/\Delta_2 = 2.1$ and $\Delta_1/\Delta_2 = 0.48$ (note that $1/0.48 = 2.1$). Such a state is realized for various ways of distributing Δ_1 and Δ_2 over the Fermi sheets,

$$C_1 = (\{a, b\}, \{b\}, \{c\}, \{a, c\}, \{c, d\}). \tag{F4}$$

All other states that are consistent with a sensitivity parameter of $\zeta \simeq 1/16$ exhibit a degree of anisotropy larger than 2.

2. General case of three gap ratios

Here, we analyze the general case of $N = 4$ in detail, where we allow for four different gap values on the four Fermi sheets $\{a, b, c, d\}$ of $PdTe_2$. As shown below, we find that the conclusions obtained from the $N = 2$ case discussed above remain unchanged.

For $N = 4$, the expression for the sensitivity parameter in Eq. (14) takes the form

$$\zeta = \frac{1}{2} - \frac{\left(1 + \sum_{j=a}^{c}\nu_j\eta_j\right)^2}{2\left(1 + \sum_{j=a}^{c}\nu_j\right)\left(1 + \sum_{j=a}^{c}\nu_j\eta_j^2\right)}, \tag{F5}$$

where $\nu_j = \rho_j/\rho_d$ and $\eta_j = \Delta_j/\Delta_d$. Note that the summations run over the three Fermi surfaces $\{a, b, c\}$. We can use Eq. (F5) to eliminate one of the η_j, say η_c, and obtain a family of solutions as a function of η_a and η_b that fulfill the condition $\zeta \simeq 1/16$ imposed by our experimental results. There are two independent solutions, $\eta_c^{\pm}(\eta_a, \eta_b)$, that differ from the sign in front of the square root ($\pm$). They need to be investigated separately.

To find the gap ratios that correspond to the most isotropic solutions, we minimize the function

$$h(\eta_a, \eta_b) = \left(\eta_a^2 - 1\right)^2 + \left(\eta_b^2 - 1\right)^2 + [\eta_c(\eta_a, \eta_b)^2 - 1]^2. \tag{F6}$$

For η_3^+ there occur three local minima. The global minimum is very close to the $C_1 = \{d\}$ isotropic A_{1g}^{+-} solution found above (see Table II):

$$\eta_1 = 1.00, \quad \eta_2 = -1.01, \quad \eta_3 = -1.02. \tag{F7}$$

One of the other two local minima corresponds to a $(+ + ++)$ solution, where the gap has the same sign on all four Fermi surfaces: $\eta_1 = -1.00$, $\eta_2 = 0.33$, $\eta_3 = 0.96$. This state, however, has a larger degree of anisotropy ($\simeq 3.0$) than that found ($\simeq 2.1$) for one gap ratio [see Eq. (F4)].

Turning to the analysis of the other solution η_c^-, we find three local minima of Eq. (F6). Two of them correspond to sign changing solutions with a larger degree of anisotropy

than the state $C_1 = \{d\}$. The third local minimum, however, corresponds to a sign preserving $(+ + ++)$ that is (slightly) more isotropic than any of the states found for one gap ratio. Specifically, its gap configuration reads

$$\eta_a = 1.00, \quad \eta_b = 1.07, \quad \eta_c = 0.51. \tag{F8}$$

Since $1/0.51 = 1.98 < 2.10$, this state is slightly less anisotropic than the solutions described by Eq. (F4). Since the reduction of the degree of anisotropy is about 6% only, however, our main conclusion, namely that the sign-preserving solutions are not consistent with the fact that $\lambda(T)$ can be described by a single gap energy scale, still holds.

[1] Ch. J. Raub, V. B. Compton, T. H. Geballe, B. T. Matthias, J. P. Maita, and G. W. Hull, Jr., J. Phys. Chem. Solids **26**, 2051 (1965).

[2] A. Kjekshus and W. B. Pearson, Can. J. Phys. **43**, 438 (1965).

[3] H.-J. Noh, J. Jeong, E.-J. Cho, K. Kim, B. I. Min, and B.-G. Park, Phys. Rev. Lett. **119**, 016401 (2017).

[4] F. Fei, X. Bo, R. Wang, B. Wu, J. Jiang, D. Fu, M. Gao, H. Zheng, Y. Chen, X. Wang, H. Bu, F. Song, X. Wan, B. Wang, and G. Wang, Phys. Rev. B **96**, 041201(R) (2017).

[5] Y. Liu, J. Z. Zhao, L. Yu, C.-T. Lin, A.-J. Liang, C. Hu, Y. Ding, Y. Xu, S.-L. He, L. Zhao, G.-D. Liu, X.-L. Dong, J. Zhang, C.-T. Chen, Z.-Y. Xu, H.-M. Weng, X. Dai, Z. Fang, and X.-J. Zhou, Chin. Phys. Lett. **32**, 067303 (2015).

[6] M. S. Bahramy, O. J. Clark, B.-J. Yang, J. Feng, L. Bawden, J. M. Riley, I. Markovic, F. Mazzola, V. Sunko, D. Biswas, S. P. Cooil, M. Jorge, J. W. Wells, M. Leandersson, T. Balasubramanian, J. Fujii, I. Vobornik, J. E. Rault, T. K. Kim, M. Hoesch, K. Okawa, M. Asakawa, T. Sasagawa, T. Eknapakul, W. Meevasana, and P. D. C. King, Nat. Mater. **17**, 21 (2017).

[7] H. Leng, C. Paulsen, Y. K. Huang, and A. de Visser, Phys. Rev. B **96**, 220506(R) (2017).

[8] S. Teknowijoyo, N. H. Jo, M. S. Scheurer, M. A. Tanatar, K. Cho, S. L. Bud'ko, P. P. Orth, P. C. Canfield, and R. Prozorov, Phys. Rev. B **98**, 024508 (2018).

[9] S. Das, Amit, A. Sirohi, L. Yadav, S. Gayen, Y. Singh, and G. Sheet, Phys. Rev. B **97**, 014523 (2018).

[10] Amit and Y. Singh, Phys. Rev. B **97**, 054515 (2018).

[11] H. Leng, J.-C. Orain, A. Amato, Y. K. Huang, and A. de Visser, Phys. Rev. B **100**, 224501 (2019).

[12] F. Rullier-Albenque, H. Alloul, and R. Tourbot, Phys. Rev. Lett. **91**, 047001 (2003).

[13] A. P. Mackenzie, R. K. W. Haselwimmer, A. W. Tyler, G. G. Lonzarich, Y. Mori, S. Nishizaki, and Y. Maeno, Phys. Rev. Lett. **80**, 161 (1998).

[14] E. C. Blomberg, M. A. Tanatar, A. Thaler, S. L. Bud'ko, P. C. Canfield, and R. Prozorov, J. Phys.: Condens. Matter **30**, 315601 (2018).

[15] S. Teknowijoyo, K. Cho, M. Konczykowski, E. I. Timmons, M. A. Tanatar, W. R. Meier, M. Xu, S. L. Bud'ko, P. C. Canfield, and R. Prozorov, Phys. Rev. B **97**, 140508(R) (2018).

[16] J. Li, Y. Guo, S. Zhang, S. Yu, Y. Tsujimoto, H. Kontani, K. Yamaura, and E. Takayama-Muromachi, Phys. Rev. B **84**, 020513(R) (2011).

[17] R. Prozorov and V. G. Kogan, Rep. Progr. Phys. **74**, 124505 (2011).

[18] M. Hoyer, S. V. Syzranov, and J. Schmalian, Phys. Rev. B **89**, 214504 (2014).

[19] A. C. Damask and G. J. Dienes, *Point Defects in Metals* (Gordon & Breach Science, London, 1963).

[20] C. T. Van Degrift, Rev. Sci. Instrum. **46**, 599 (1975).

[21] R. Prozorov and R. W. Giannetta, Supercond. Sci. Technol. **19**, R41 (2006).

[22] A. A. Abrikosov and L. P. Gorkov, Zh. Eksp. Teor. Fiz. **39**, 1781 (1960) [Sov. Phys. JETP **12**, 1243 (1961)].

[23] P. Anderson, J. Phys. Chem. Solids **11**, 26 (1959).

[24] A. A. Abrikosov and L. P. Gorkov, Zh. Eksp. Teor. Fiz. **35**, 1558 (1958) [Sov. Phys. JETP **8**, 1090 (1959)].

[25] A. A. Abrikosov and L. P. Gorkov, Zh. Eksp. Teor. Fiz. **36**, 319 (1959) [Sov. Phys. JETP **9**, 220 (1959)].

[26] G. Chanin, E. A. Lynton, and B. Serin, Phys. Rev. **114**, 719 (1959).

[27] D. Markowitz and L. P. Kadanoff, Phys. Rev. **131**, 563 (1963).

[28] P. Hohenberg, Zh. Eksp. Teor. Fiz. **45**, 1208 (1963) [Sov. Phys. JETP **18**, 834 (1964)].

[29] R. Balian and N. R. Werthamer, Phys. Rev. **131**, 1553 (1963).

[30] S. Maekawa, Y. Isawa, and H. Ebisawa, Jpn. J. Appl. Phys. **26**, L771 (1987).

[31] R. J. Radtke, K. Levin, H.-B. Schüttler, and M. R. Norman, Phys. Rev. B **48**, 653(R) (1993).

[32] A. A. Golubov and I. I. Mazin, Phys. Rev. B **55**, 15146 (1997).

[33] K. Maki and E. Puchkaryov, Europhys. Lett. **45**, 263 (1999).

[34] V. G. Kogan, Phys. Rev. B **80**, 214532 (2009).

[35] R. H. T. Wilke, S. L. Budko, P. C. Canfield, J. Farmer, and S. T. Hannahs, Phys. Rev. B **73**, 134512 (2006).

[36] Y. Bang and G. R. Stewart, J. Phys.: Condens. Matter **29**, 123003 (2017).

[37] I. I. Mazin and J. Schmalian, Physica C **469**, 614 (2009).

[38] Y. Senga and H. Kontani, J. Phys. Soc. Jpn. **77**, 113710 (2008).

[39] S. Onari and H. Kontani, Phys. Rev. Lett. **103**, 177001 (2009).

[40] Y. Wang, A. Kreisel, P. J. Hirschfeld, and V. Mishra, Phys. Rev. B **87**, 094504 (2013).

[41] K. Michaeli and L. Fu, Phys. Rev. Lett. **109**, 187003 (2012).

[42] D. C. Cavanagh and P. M. R. Brydon, Phys. Rev. B **101**, 054509 (2020).

[43] M. S. Scheurer, M. Hoyer, and J. Schmalian, Phys. Rev. B **92**, 014518 (2015).

[44] M. Hoyer, M. S. Scheurer, S. V. Syzranov, and J. Schmalian, Phys. Rev. B **91**, 054501 (2015).

[45] M. S. Scheurer, Ph.D. thesis, Karlsruher Institut für Technologie (KIT), 2016.

[46] M. A. Tanatar, A. E. Böhmer, E. I. Timmons, M. Schütt, G. Drachuck, V. Taufour, K. Kothapalli, A. Kreyssig, S. L. Bud'ko, P. C. Canfield, R. M. Fernandes, and R. Prozorov, Phys. Rev. Lett. **117**, 127001 (2016).

[47] M. A. Tanatar, V. A. Bondarenko, E. I. Timmons, and R. Prozorov, Rev. Sci. Instrum. **89**, 013903 (2018).

[48] R. Prozorov, R. W. Giannetta, A. Carrington, and F. M. Araujo-Moreira, Phys. Rev. B **62**, 115 (2000).

[49] Y. Mizukami, Y. Konczykowski, M. Kawamoto, S. Kurata, S. Kasahara, K. Hashimoto, V. Mishra, Y. Kreisel, A. Wang, P. J.

Hirschfeld, Y. Matsuda, and T. Shibauchi, Nat. Commun. **5**, 5657 (2014).
[50] K. Cho, M. Kończykowski, S. Teknowijoyo, M. A. Tanatar, and R. Prozorov, Supercond. Sci. Technol. **31**, 064002 (2018).
[51] M. W. Thompson, *Defects and Radiation Damage in Metals* (Cambridge University Press, Cambridge, UK, 1974), p. 142.
[52] A. Pippard, in *Magnetoresistance in Metals*, edited by A. Goldman, P. McClintock, and M. Springford (Cambridge University Press, Cambridge, UK, 1989).
[53] J. Paglione, M. A. Tanatar, D. G. Hawthorn, F. Ronning, R. W. Hill, M. Sutherland, L. Taillefer, and C. Petrovic, Phys. Rev. Lett. **97**, 106606 (2006).
[54] H. Shakeripour, C. Petrovic, and L. Taillefer, New J. Phys. **11**, 055065 (2009).
[55] A. Lavasani, D. Bulmash, and S. Das Sarma, Phys. Rev. B **99**, 085104 (2019).
[56] M. Sigrist and K. Ueda, Rev. Mod. Phys. **63**, 239 (1991).
[57] C. B. Satterthwaite, Phys. Rev. **125**, 873 (1962).
[58] H. Shakeripour, M. A. Tanatar, S. Y. Li, C. Petrovic, and L. Taillefer, Phys. Rev. Lett. **99**, 187004 (2007).
[59] H. Shakeripour, M. A. Tanatar, C. Petrovic, and L. Taillefer, Phys. Rev. B **82**, 184531 (2010).
[60] L. Taillefer, B. Lussier, R. Gagnon, K. Behnia, and H. Aubin, Phys. Rev. Lett. **79**, 483 (1997).
[61] M. Suzuki, M. A. Tanatar, N. Kikugawa, Z. Q. Mao, Y. Maeno, and T. Ishiguro, Phys. Rev. Lett. **88**, 227004 (2002).
[62] J. R. Schrieffer, *Theory of Superconductivity* (Westview, Boulder, 1999).
[63] M. Tinkham, *Introduction to Superconductivity*, 2nd ed. (Dover, New York, 1996).
[64] R. Prozorov, M. Kończykowski, M. A. Tanatar, A. Thaler, S. L. Bud'ko, P. C. Canfield, V. Mishra, and P. J. Hirschfeld, Phys. Rev. X **4**, 041032 (2014).
[65] P. J. Hirschfeld, C. R. Phys. **17**, 197 (2016).
[66] K. Cho, M. Kończykowski, J. Murphy, H. Kim, M. A. Tanatar, W. E. Straszheim, B. Shen, H. H. Wen, and R. Prozorov, Phys. Rev. B **90**, 104514 (2014).
[67] Y. Mizukami, M. Konczykowski, K. Matsuura, T. Watashige, S. Kasahara, Y. Matsuda, and T. Shibauchi, J. Phys. Soc. Jpn. **86**, 083706 (2017).
[68] P. Blaha, K. Schwarz, G. K. H. Madsen, D. Kvasnicka, J. Luitz, R. Laskowski, F. Tran, and L. D. Marks, *WIEN2k: An Augmented Plane Wave plus Local Orbitals Program for Calculating Crystal Properties* (Vienna University of Technology, Austria, 2018).
[69] M. S. Scheurer, Phys. Rev. B **93**, 174509 (2016).
[70] X.-L. Qi, T. L. Hughes, and S.-C. Zhang, Phys. Rev. B **81**, 134508 (2010).
[71] L. Andersen, A. Ramires, Z. Wang, T. Lorenz, and Y. Ando, Sci. Adv. **6**, eaay6502 (2020).
[72] A. A. Abrikosov, L. P. Gorkov, and I. E. Dzyaloshinski, *Methods of Quantum Field Theory in Statistical Physics* (Dover, New York, 1975), revised English ed.
[73] M. S. Scheurer, D. F. Agterberg, and J. Schmalian, npj Quantum Mater. **2**, 9 (2017).
[74] L. Ke, Phys. Rev. B **99**, 054418 (2019).
[75] N. Marzari and D. Vanderbilt, Phys. Rev. B **56**, 12847 (1997).
[76] A. A. Mostofi, J. R. Yates, G. Pizzi, Y.-S. Lee, I. Souza, D. Vanderbilt, and N. Marzari, Comput. Phys. Commun. **185**, 2309 (2014).
[77] I. Souza, N. Marzari, and D. Vanderbilt, Phys. Rev. B **65**, 035109 (2001).
[78] N. Marzari, A. A. Mostofi, J. R. Yates, I. Souza, and D. Vanderbilt, Rev. Mod. Phys. **84**, 1419 (2012).
[79] W. Kim, G. Chao, and L. Cabri, J. Less Common Met. **162**, 61 (1990).
[80] J. P. Perdew, K. Burke, and M. Ernzerhof, Phys. Rev. Lett. **77**, 3865 (1996).
[81] One might think that the generalized Anderson theorem should hold upon projecting the order parameter onto the low-energy basis, without the need of an extra symmetry. Then, indeed, Eq. (8a) will be satisfied. However, the projection will affect the commutation properties between the disorder potential and the order parameter; without additional symmetries of the Hamiltonian, Eq. (8b) will become invalid as can be easily verified.